

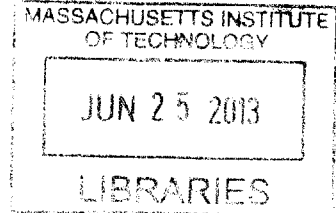
Surface Structural Changes of Perovskite Oxides during Oxygen Evolution in Alkaline Electrolyte

ARCHIVES

by

Kevin J. May

B.Eng., Engineering Physics, McMaster University (2010)



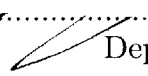
SUBMITTED TO THE DEPARTMENT OF MECHANICAL ENGINEERING
IN PARTIAL FULFILLMENT OF THE REQUIREMENTS FOR THE DEGREE OF
MASTER OF SCIENCE IN MECHANICAL ENGINEERING

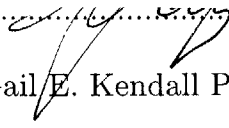
at the

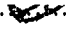
MASSACHUSETTS INSTITUTE OF TECHNOLOGY

June 2013

© 2013 Massachusetts Institute of Technology
All rights reserved.

Signature of Author.....

Department of Mechanical Engineering
May 10, 2013

Certified by.....

Yang Shao-Horn
Gail E. Kendall Professor of Mechanical Engineering
Thesis Supervisor

Accepted by.....

David E. Hardt
Ralph E. and Eloise F. Cross Professor of Mechanical Engineering
Chairman, Department Graduate Committee

Surface Structural Changes of Perovskite Oxides during
Oxygen Evolution in Alkaline Electrolyte

by

Kevin J. May

Submitted to the Department of Mechanical Engineering
on May 10, 2013 in Partial Fulfillment of the
Requirements for the Degree of Master of Science in
Mechanical Engineering

Abstract

Perovskite oxides such $\text{Ba}_{0.5}\text{Sr}_{0.5}\text{Co}_{0.8}\text{Fe}_{0.8}\text{O}_{3-\delta}$ (BSCF82) are among the most active catalysts for the oxygen evolution reaction (OER) in alkaline solution reported to date. In this work it is shown via high resolution transmission electron microscopy (HRTEM) and Raman spectroscopy that oxides such as BSCF82 rapidly undergoes amorphization at its surface under OER conditions, which occurs simultaneously with an increase in the pseudocapacitive current and OER activity. This amorphization was not detected at potentials below those where significant OER current was observed. Lower concentrations of Sr^{2+} and Ba^{2+} are found in the amorphous regions of BSCF82. Perovskite oxides with lower OER activities such as LaCoO_3 (LCO) and LaMnO_3 (LMO) remained crystalline under identical electrochemical conditions. In addition, the OER activity and tendency for amorphization are found to correlate with the oxygen p -band center as calculated using density functional theory. This work illustrates that the surface structure and stoichiometry of oxide catalysts can differ significantly from the bulk during catalysis, and that understanding these phenomena is critical for designing highly active and stable catalysts for the OER.

Thesis Supervisor: Yang Shao-Horn

Title: Gail E. Kendall Professor of Mechanical Engineering

List of Publications

1. Grimaud, A., Carlton, C.E., Risch, M., Hong, W.T., **May, K.J.** & Shao-Horn, Y. On the Influence of Cobalt and Manganese Coordination on the Catalytic Activity of Perovskites for Oxygen Evolution. *Submitted*.
2. Grimaud, A., **May, K.J.**, Carlton, C.E., Lee, Y.-L., Risch, M., Zhou, J. & Shao-Horn, Y. Double Perovskites as a New Family of Highly Active Catalysts For Oxygen Evolution in Alkaline Solution. *Submitted*.
3. Ming, T., Suntivich, J., **May, K.J.**, Stoerzinger, K.A. & Shao-Horn, Y. Visible Light Photo-Oxidation in Au Nanoparticle Sensitized SrTiO₃:Nb Photoanode. *Submitted*.
4. Risch, M., Grimaud, A., **May, K.J.**, Stoerzinger, K.A., Chen, T.J., Mansour, A.N., & Shao-Horn, Y. Structural Changes of Cobalt-based Perovskites upon Water Oxidation Investigated by EXAFS. *The Journal of Physical Chemistry C* **117**, 8628-8635 (2013).
5. **May, K. J.**, Carlton, C.E., Stoerzinger, K.A., Risch, M., Suntivich, J., Lee, Y.-L., Grimaud, A., & Shao-Horn, Y. The Influence of Oxygen Evolution during Water Oxidation on the Surface of Perovskite Oxide Catalysts. *The Journal of Physical Chemistry Letters* **3**, 3264-3270 (2012).
6. Lee, Y., Suntivich, J., **May, K. J.**, Perry, E. E. & Shao-Horn, Y. Synthesis and Activities of Rutile IrO₂ and RuO₂ Nanoparticles for Oxygen Evolution in Acid and Alkaline Solutions. *The Journal of Physical Chemistry Letters* **3**, 399-404 (2012).
7. Suntivich, J., **May, K. J.**, Gasteiger, H. A., Goodenough, J. B. & Shao-Horn, Y. A Perovskite Oxide Optimized for Oxygen Evolution Catalysis from Molecular Orbital Principles. *Science* **334**, 1383-1385 (2011).

Acknowledgements

I would first like to acknowledge my advisor, Professor Yang Shao-Horn, for not only her academic and research-oriented guidance but also for giving unwavering support in all other aspects of my graduate career. You have believed in my abilities as a student and researcher, and fostered my independence and creativity; I have learned so much more than just science and research during my time at MIT because of this. Thank you.

Funding for this work is gratefully acknowledged. Support was received from the MRSEC Program of the National Science Foundation (DMR-0819762), Eni S.p.A. under the Eni-MIT Alliance Solar Frontiers, and the DOE Hydrogen Initiative Program (DE-FG02-05ER15728). I also received support from the Natural Sciences and Engineering Research Council of Canada (PGS-M).

I would like to also extend my appreciation and thanks to my fellow lab members in the Electrochemical Energy Lab for their friendship and support. Both present and past, the students and postdoctoral researchers in this group are the best I could ever imagine working with. I appreciate the support of everyone in the group, and would like to mention some members in particular who have contributed to the scientific work in this thesis: Jin Suntivich, for his enthusiasm in teaching the fundamentals of electrochemistry and for providing mentorship when I was beginning my graduate studies, which significantly shaped my way of scientific thinking and how I approach research; Chris Carlton, for his TEM expertise and helpful discussions in the broader subject of materials science; Kelsey Stoerzinger for her Raman spectroscopy contributions; Marcel Risch for assisting in electrode preparation for Raman spectroscopy and for his expertise in amorphous cobalt oxides and electrochemistry; Yueh-Lin Lee for density functional theory calculations, and Alexis Grimaud for always-helpful discussions in solid state chemistry and synthesis of perovskite oxide compounds.

I also thank my family for their love and support, for making me the person I am today and also for giving me all the opportunities I needed to succeed. My parents never faltered in fostering my curiosity and encouraging me unconditionally in my endeavors. To Megan and Brandon, I'm lucky to have you as siblings, and I know I can always rely on you for support.

Finally, I want to give my love and gratitude to Sana, for being my other half through thick and thin. You have given me the strength and confidence to persevere through any challenges that arise. This has helped me so much, perhaps even more than you know. Thank you for being who you are and for being my partner in everything.

Table of Contents

Abstract	3
List of Publications	5
Acknowledgements	7
List of Figures	11
List of Tables	15
1 Introduction	17
1.1 Motivation	17
1.2 The Oxygen Evolution Reaction: Historical Overview	18
1.3 Perovskite Oxides as Oxygen Evolution Catalysts	23
1.4 Scope of this Thesis.....	26
2 Experimental	29
2.1 Oxide Synthesis and Characterization.....	29
2.2 Electrode Preparation	31
2.3 Electrochemical Measurements.....	31
2.4 Characterization of Electrochemically-Cycled Electrodes	32
2.5 Density Functional Theory Calculations	34
3 Results and Discussion	35
3.1 Material Characterization	35
3.2 Electrochemical Measurements.....	37
3.3 Transmission Electron Microscopy	42
3.4 Raman Spectroscopy and Potential-Dependent Amorphization	48
3.5 Amorphization and Pseudocapacitive Current	51
3.6 O <i>p</i> -band Center: A Descriptor from Density Functional Theory	54
4 Conclusions and Looking Forward	57
5 References	61

List of Figures

- Figure 1.1:** Free energies of OER intermediates on an oxide surface, for the case of zero applied potential and 1.23 V applied potential. The specific intermediates assumed are not considered here. The “ideal” catalyst is shown in red, while a more realistic catalyst is shown in blue. The ideal catalyst has a flat energy landscape at the thermodynamic equilibrium potential of 1.23 V vs. RHE. Figure adapted from work by Rossmeisl et al.²⁵ and Dau et al.¹⁶23
- Figure 1.2:** Cubic perovskite structure. The central B-site transition metal (dark blue) is octahedrally coordinated by oxygen (red), with the A-site alkaline earth or lanthanide metal (yellow) at the corners in a 12-fold coordination by oxygen.24
- Figure 1.3:** Qualitative molecular orbital diagram for octahedrally-coordinated transition metal ion. Asterisks denote antibonding states. In bold are the e_g and t_{2g} states of interest in catalysis. Figure adapted from Cox.⁷⁶25
- Figure 1.4:** Volcano plot showing the relationship between OER catalytic activity, defined as the overpotential at $50 \mu\text{A cm}^{-2}$ (estimated true oxide surface area), and the e_g orbital occupancy of the B-site transition metal ion. Figure from previous work.¹⁰26
- Figure 3.1:** X-ray diffraction data for the oxides studied in this work. LMO, LCO data were gathered by Jin Suntivich. LSC46 data were gathered by Ethan J. Crumlin. SCF82 data were gathered by Alexis Grimaud.35
- Figure 3.2:** Experimental XRD peak locations (red) with database peak positions for LSC46 (gray) and Si (green). Si was included to give reference diffraction peaks.36
- Figure 3.3:** Cyclic voltammetry for (a) LMO, (b) LCO, (c) LSC46, (d) BSCF46, (e) BSCF82 and (f) SCF82. Number labels n indicate the n^{th} cycle of cyclic voltammetry (1.1-1.7 V versus RHE, 10 mV/s). All measurements were performed in O_2 -saturated 0.1 M KOH, corrected for ohmic losses and normalized to the SEM-estimated surface area of oxides, and used an oxide loading of 0.25 mg/cm^2 supported on glassy carbon. Figure adapted from published work.¹¹38
- Figure 3.4:** Heavy cycling of (a) BSCF82 and (b) LSC46; (c) Potentiostatic measurements on BSCF82, LSC46, LCO and LMO; (d) Tafel plot containing cyclic voltammetry at the n^{th} cycles (hollow markers) and potentiostatic data (solid markers) for comparison. Figure adapted from published work.¹¹39
- Figure 3.5:** Capacitance- and ohmic-corrected cyclic voltammogram data (1.0-1.7 V versus RHE, 10 mV/s) of a BSCF82 electrode (0.25 mg/cm^2 oxide loading) on the first cycle (blue line). Also shown are potentiostatic data on the same electrode taken

immediately after the first cycle (red X). Measurements taken in O₂-saturated 0.1 M KOH, normalized to geometric electrode area. Figure adapted from published work.¹¹..40

Figure 3.6: Selected regions of the data shown in Figure 3.4a. Data are capacitance- and iR-corrected. For each cycle, the average of the forward and backward scan was mirrored in time to account for current from both forward and backward scans. Figure adapted from published work.¹¹41

Figure 3.7: Potentiostatic data measured on a single BSCF82 electrode, held at 1.6 V vs. RHE for 2 h. This electrode did not contain AB carbon. Measurement performed by Marcel Risch. Figure adapted from published work.¹¹42

Figure 3.8: HRTEM and FFTs from approximately 35 × 35 nm areas of (a) as-prepared BSCF82, (b) cycled BSCF82, (c) as-prepared LMO, (d) cycled LMO, (e) as-prepared LCO, (f) cycled LCO, (g) as-prepared LSC46 and (h) cycled LSC46. Cycling consisted of five cycles between 1.1-1.7 V vs. RHE in O₂-saturated 0.1 M KOH at 10 mV/s. HRTEM performed by Christopher E. Carlton. Figure adapted from published work.¹¹43

Figure 3.9: HRTEM and FFTs of (a) as-prepared BSCF82 powder, (b) BSCF82 cycled 5 times, (c) BSCF82 cycled 185 times, (d) as-prepared BSCF46, (e) BSCF46 cycled 5 times, and (f) LSC46 cycled 185 times. Cycles were 1.1-1.7 V vs. RHE at 10 mV/s, in O₂-saturated 0.1 M KOH. HRTEM performed by Christopher E. Carlton. Figure adapted from published work.¹¹44

Figure 3.10: HRTEM and FFT of BSCF82 electrode that was cycled 5 times (a) with AB carbon and (b) without AB carbon. The amorphous layers are similar and show that AB carbon does not significantly contribute to the amorphization process. HRTEM performed by Christopher E. Carlton. Figure adapted from published work.¹¹.....44

Figure 3.11: HRTEM and corresponding FFTs of particle surfaces of (a) as-prepared BSCF82, (b) BSCF82 cycled 5 times, (c) BSCF82 cycled 100 times, (d) BSCF82 held potentiostatically at 1.7 V vs. RHE for 2 h, and (e) SCF82 cycled 5 times. Cycles were 1.1-1.7 V vs. RHE at 10 mV/s, in O₂-saturated 0.1 M KOH. HRTEM performed by Christopher E. Carlton. Figure adapted from published work.¹¹.....45

Figure 3.12: High angular annular dark field imaging and scanning TEM EDS of BSCF82 cycled 5 times between 1.1-1.7 V vs. RHE at 10 mV/s, in O₂-saturated 0.1 M KOH. The quantitative EDS results are shown in both the images (a) and (b), and plotted vs. the distance from the particle edge in (c) and (d). Both (a) and (b) are the same image, with EDS taken at different locations on the particle. A-site atom concentration (Ba and Sr) is compared to B-site concentration (Co and Fe) for visual clarity. HRTEM/EDS performed by Christopher E. Carlton. Figure adapted from published work.¹¹46

Figure 3.13: Co_3O_4 peaks have been observed in the Raman spectra of both BSCF82 and LSC46, both cycled 5 times between 1.1-1.7 V vs. RHE at 10 mV/s. The multipliers in the image refer to intensity scaling for visual clarity. Approximately 15% of spectra exhibited the Co_3O_4 -like peaks. These peaks were never observed for as-prepared samples, nor in LCO samples before or after cycling. Raman spectroscopy performed by Kelsey A. Stoerzinger. Figure adapted from published work.¹¹47

Figure 3.14: Raman spectra of (a) BSCF82 and (b) LCO before and after cycling 5 and 50 times, (c) BSCF82 after cycling 50 times in the indicated voltage windows, (d) LMO, (e) LSC46 and (f) BSCF46 before and after cycling 5 and 50 times. Cycling took place in O_2 -saturated 0.1 M KOH at 10 mV/s. Raman spectroscopy performed by Kelsey A. Stoerzinger. Figure adapted from published work.¹¹49

Figure 3.15: Raman spectra (left) of BSCF82 after potentiostatically holding at the labeled potential until 27.4 mC of charge had passed. Electrochemical data is shown on the right panel. Times required were 0.06, 1.78, and 24 h for 1.600 (red), 1.475 (green) and 1.45 (blue) V vs. RHE, respectively. For potentials with appreciable OER current, the current increased over time, accompanying more drastic changes in the Raman spectra. Raman spectroscopy performed by Kelsey A. Stoerzinger. Figure adapted from published work.¹¹50

Figure 3.16: Oxygen evolution current at 1.58 V vs. RHE vs. the cathodic charge passed during a single cycle (1.1-1.7 V vs. RHE, 10 mV/s) in 0.1 M KOH. Cycle numbers are labeled. Inset shows a single cycle (5th) with the shaded region being proportional to the cathodic charge. Figure adapted from published work.¹¹52

Figure 3.17: Tafel plots for BSCF82 (solid squares, 2nd cycle; open squares, 185th cycle) and an electrochemically-deposited amorphous Co oxide film (green triangle, 2nd cycle) in 0.1 M KOH. Tafel plots constructed from averaged forward-backward scans of cyclic voltammetry (10 mV/s) and normalized to the total number of Co in bulk or on the surface. BSCF82 data was gathered on a single electrode while the Co film data was the average of 5 independent measurements (250 nmol/cm²_{disk} loading, 200 nm thick). The number of cobalt atoms in BSCF82 was estimated from the formula unit, mass loading and SEM-estimated surface area. For the Co-film, the number of Co ions was estimated from the Faradaic charge passed during electrodeposition at 0.806 V vs. SCE in 0.1 M potassium phosphate (pH 7), assuming all charge was due to Co^{2+} to Co^{3+} oxidation. Co film data was gathered by Marcel Risch. Figure adapted from published work.¹¹53

Figure 3.18: (a) Calculated O *p*-band centers of perovskites BSCF46, BSCF82, SCF82, LSC46, LCO and LMO, and (b) the overpotentials at 0.25 mA/cm²_{ox}. Stoichiometry in the calculations is not exact due to the coarse composition grid in the simulated supercells. Oxides represented with red bars exhibit rapid surface amorphization during water oxidation, while those represented with blue bars remain highly crystalline. DFT performed by Yueh-Lin Lee. Figure adapted from published work.¹¹55

List of Tables

Table 3.1: Space groups and lattice parameters of the oxides studied in this work.....36

Table 3.2: SEM-estimated surface areas of oxides in this work.....36

1 Introduction

1.1 Motivation

The risks of anthropogenic climate change have led to intensive research towards alternative sources of energy to conventional fossil fuels. Greenhouse gas emissions have steadily increased and are projected to continue to increase in the near future,^{1,2} further highlighting the need for scientific solutions to the global energy crisis. Clean, renewable energy sources such as wind and solar energy have attracted significant attention, but have the disadvantage of being intermittent in nature. One possible avenue to improving the reliability and practicality of these technologies is a robust and efficient way of storing intermittent energy as chemical fuel which can be used at a later time. In particular, molecular hydrogen generated by the electrochemical splitting of water has received a large amount of focus in the literature.³⁻¹¹ However, the efficiency of this process is limited by the sluggish electrochemical kinetics of the oxygen evolution reaction (OER), which is one half of the overall water splitting reaction (the other half being the hydrogen evolution reaction, HER).

Commercial grid electrolyzers are attractive for their simplicity and commercial readiness compared to the direct solar-to-fuel scheme.¹² While larger-scale systems will start to accumulate ohmic losses that make up a large part of the efficiency losses, kinetic overpotential loss from the oxygen evolution reaction still remains significant¹³ and necessitates the use of precious metal oxides (IrO_2 , RuO_2) for acidic electrolytes¹⁴ and nickel/nickel oxides which are susceptible to deactivation over time in alkaline electrolytes.¹²

There has been growing interest in the area of solar fuels,^{4,6} where sunlight is used to drive the synthesis of chemical fuel, in a sort of “artificial photosynthesis”. For these applications, where current density is limited by the solar photon flux, highly efficient catalysts may be particularly important as a way to reduce the photovoltage needed to sustain a given current, relaxing constraints on semiconductor device performance. The state-of-the-art OER catalysts typically require around 400 mV of overpotential^{5,10} to sustain the current densities achieved in record photoelectrochemical cells.¹⁵ This is a non-trivial amount of additional photovoltage for a device to provide.

It is clear that earth-abundant, inexpensive and highly efficient catalysts for the OER will have an enormous impact on the viability of generating hydrogen from water, and possibly for the generation of other hydrocarbon fuels as well, where the OER is a half-reaction. However, the exact mechanism remains relatively poorly understood (i.e. when compared to HER), even though there have been recent advances in achieving high-performance catalysts with some first steps towards rational design.^{3,7,10,11} There remains much room for furthering our fundamental understanding of the reaction mechanism and the requirements for a highly active, stable catalyst.

1.2 The Oxygen Evolution Reaction: Historical Overview

The OER is a 4 step, 4 electron transfer half-reaction, with the net reaction typically written in acid as $(2\text{H}_2\text{O} \rightarrow \text{O}_2 + 4\text{H}^+ + 4\text{e}^-)$ ^{16,17} and in alkaline as $(4\text{OH}^- \rightarrow 2\text{H}_2\text{O} + \text{O}_2 + 4\text{e}^-)$.^{18,19} The slow kinetics of this reaction have been known—albeit not fully understood—for nearly a century, along with the fact that the metal electrodes

studied frequently in early reports from oxide layers under OER conditions.²⁰⁻²³ Hoar proposed²⁰ that the electrochemical irreversibility is due to the permeability of the oxide film to electrolyte and the resulting self-polarization (not taking into consideration electrode kinetics), and mentions that a hypothetical catalytically-active stable metal surface could provide reversible electrochemical behavior—although this is not possible to test experimentally and is not in agreement with the modern picture of OER irreversibility based on density functional theory.²⁴⁻²⁶ Hoar was also the first to make the connection that the intersection of the Tafel lines for oxygen evolution and reduction occurs at 1.23 V vs. reversible hydrogen electrode (RHE), which is the theoretical thermodynamic potential.²⁰ One study by Bockris²³ treated the OER (and multi-step electron transfer reactions in general) in an analogous manner to the much more widely studied hydrogen electrode, which by that time was starting to be understood to be governed by the binding strength of intermediate hydrogen species to the catalyst surface.²⁷ Bockris performed a theoretical analysis of the expected Tafel behavior of a series of hypothetical reaction pathways, by first expressing rate equations for each step in the OER, and making several assumptions on the coverage isotherm, species concentrations and rate-limiting step.²³ This allowed a table of theoretical Tafel slopes to be generated for a series of proposed pathways, for comparison to experimental data. Unfortunately, the Tafel slopes were not unique to each proposed mechanism and therefore we cannot determine, from this type of analysis, the true mechanism of the OER—which to this day is still not conclusively understood.

Other early work focused on the attainability of a “reversible” oxygen electrode, especially in acidic solution with platinum working electrodes and careful elimination of

system impurities.^{18,28-34} Here, “reversible” refers to observing an open-circuit potential equal to the thermodynamic potential of 1.23 V vs. RHE. This is indeed attainable on clean platinum electrodes with electrolytes that have been pre-electrolyzed to achieve low impurity concentrations, however, once appreciable OER current begins, the anodic oxidation of platinum stops the reversible behavior.^{18,35} In general, the open circuit potential of approximately 1.0 V vs. RHE typically seen on platinum electrodes, is attributed to a competing process, or mixed potential, between oxygen reduction (for which Pt is a good catalyst) and platinum oxidation, owing to the extremely slow OER kinetics.³⁴ With this in mind, it is important to distinguish between a surface that can provide an open circuit potential near the thermodynamically reversible potential and a surface that can sustain high OER current with low overpotential. Platinum was therefore only of interest as a model surface for fundamental studies of the OER mechanism in acidic electrolyte.

Other electrodes, such as precious-metals iridium and ruthenium, have also been investigated.³⁶⁻³⁹ Shortly thereafter, the highly-active rutile oxide catalysts IrO₂ (used in proton exchange membrane electrolyzers) and RuO₂ were discovered.^{40,41} These materials have still been subjects of active research in recent times.^{5,37,42-46} These oxides reigned as the most-active OER catalysts until recently,¹⁰ when transition metal oxides were demonstrated to be capable of exceeding precious-metal oxides in activity. Transition metal electrodes (their oxidized surfaces) have also been measured,^{19,47-56} including perovskite oxides, which will be discussed further in the next section. Typically these systems are more complicated than the metal surfaces frequently studied in hydrogen

evolution/oxidation and less can be said of the exact nature of the oxygen electrocatalysis mechanisms on these surfaces based on the electrochemistry data alone.¹⁶ The mechanism may very well change between different materials. Investigating transition metal oxide catalysts for OER remains an active area of study.

Recently, focus has increased on amorphous or nano-structured cobalt and nickel oxides as OER catalysts, deposited anodically in phosphate or borate buffer solution.^{7,16,57-61} Notably, these catalysts have a self-repairing ability in the above-mentioned buffer solutions and have high catalytic activity even in neutral pH. Furthermore, when comparing films of different thickness, the activity increases, suggesting that the oxide films are permeable to electrolyte and that cobalt sites within the bulk of the material are capable of acting as active sites for the OER.⁶² Preliminary isotope labeling experiments via ¹⁸O-rich oxide films revealed significant amounts of ³⁵O₂ and ³⁶O₂ from in-line mass spectrometry, hinting that bulk oxygen may play a role in the OER mechanism.⁶² Structural studies of amorphous cobalt films via extended X-ray absorption fine structure (EXAFS) have revealed that the bulk film is composed of structural motifs or “clusters”, consisting of interconnected Co³⁺-oxo cubanes, with cobalt in edge-sharing octahedra.^{63,64} It has been suggested from this structure that the space between clusters could be filled with cations, anions or water, giving structural evidence for the possibility of bulk cobalt atoms being active for OER.¹⁶ Furthermore, the activity seems to scale with the size of these clusters.^{57,65} These amorphous, electrochemically-deposited oxide films are of importance not only as potentially viable catalysts in commercial applications, but also for the new fundamental insights that may be gained through their study.

This section ends with a discussion of recent developments in the understanding of OER kinetics. Perhaps one of the most profound advances in the study of oxygen electrocatalysis—or electrocatalysis in general—is the “volcano” plot, first introduced from theoretical considerations by Balandin.⁶⁶ This is a visual representation of Sabatier’s principle: the optimal catalyst will bind the adsorbed species neither too strongly nor too weakly.⁶⁷ Trasatti presented an experimental volcano plot from the literature available at the time for the oxygen evolution reaction, with the experimental OER overpotential at a given current plotted versus the heat of formation from a lower oxide to a higher oxide (where the metal becomes more oxidized) for the various metals, effectively giving a measure of the metal-oxygen bond strength.⁶⁸ This has led to a thermodynamic picture of catalysis, where catalytic activity is described in terms of the binding strength of intermediate species in the overall reaction.⁶⁹ In this framework, the change in Gibbs free energy of adsorbed intermediates must be energetically downhill for each reaction step in order for the overall reaction to proceed appreciably.⁶⁹ In the ideal case, each intermediate step would result in a change of Gibbs free energy of 1.23 eV, such that when the electrode potential is 1.23 V vs. RHE, the energy landscape is flat (Figure 1.1). Some development of this concept was done via density functional theory calculations of the binding strength of oxygen intermediates on various surfaces. Rossmeisl et al. found scaling relationships between related oxygen intermediate species.^{24,25} This means that the adsorption energy of $-OOH$ and $-OH$, for example, are not independent. In the context of the thermodynamic framework described above, this implies that there is a limit to the activity of an OER catalyst.⁶⁹ In real systems the

changes in Gibbs free energy for different intermediates are not the same, and since they are not independent of each other they cannot be individually tailored to give the ideal binding strength (Figure 1.1). It is important to note that this framework does not take into account transition states, only intermediates bound to the surface, and hence it does not truly consider kinetics. It remains to be seen whether such scaling relationships can be overcome by creative catalyst design, such as three-dimensional structures or multiple types of active site.

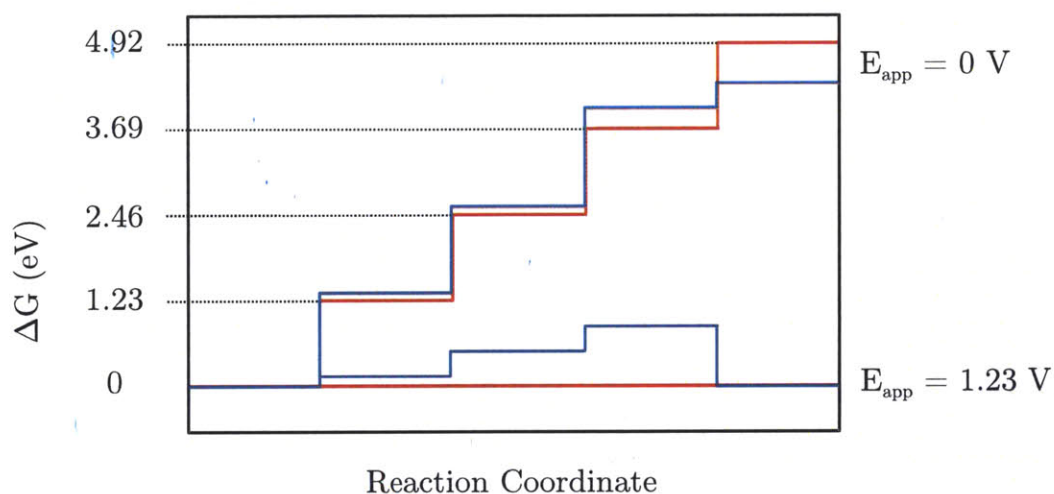


Figure 1.1: Free energies of OER intermediates on an oxide surface, for the case of zero applied potential and 1.23 V applied potential. The specific intermediates assumed are not considered here. The “ideal” catalyst is shown in red, while a more realistic catalyst is shown in blue. The ideal catalyst has a flat energy landscape at the thermodynamic equilibrium potential of 1.23 V vs. RHE. Figure adapted from work by Rossmeisl et al.²⁵ and Dau et al.¹⁶

1.3 Perovskite Oxides as Oxygen Evolution Catalysts

Perovskites are a diverse set of compounds typically with formula ABO_3 , where A is typically an alkaline earth or lanthanide metal but can be monovalent, bivalent or trivalent, and B a transition metal with the ideal cubic structure shown in Figure 1.2.⁷⁰ The A-site is 12-fold coordinated with oxygen and the B-site is in an octahedral 6-fold

coordination with oxygen. Ideally, the B-O distance is $a/2$, where a is the cubic unit cell length, and the A-O distance is $a/\sqrt{2}$, giving a Goldschmidt tolerance factor⁷¹ of 1:

$$t = \frac{(r_A + r_O)}{\sqrt{2}(r_B + r_O)} \quad (1.1)$$

For perovskites with $t \approx 1$, and at high temperatures, the structure is usually cubic. Deviations from $t = 1$ can result in different distortions of the structure, such as orthorhombic or rhombohedral. Perovskites are incredibly useful as a set of model compounds owing to the large variety in chemistry and structure available by changing the A- and B-site cations and by changing the stoichiometry via alloying. They have therefore been used in many studies for oxygen electrocatalysis.^{10,72-76}

Typically in electrocatalysis the ion of interest is the B-site, and is usually assumed to be the active site for oxygen evolution.^{10,73} From a crystal field theory perspective, the octahedrally-coordinated B-site's d -state manifold will be split into several levels, as shown in Figure 1.3. The states of interest for catalysis will be the antibonding e_g and t_{2g} states, since they are typically the occupied states with highest energy and their filling will roughly determine the strength of the B-O bond.^{72,77}

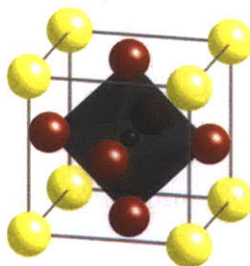


Figure 1.2: Cubic perovskite structure. The central B-site transition metal (dark blue) is octahedrally coordinated by oxygen (red), with the A-site alkaline earth or lanthanide metal (yellow) at the corners in a 12-fold coordination by oxygen.

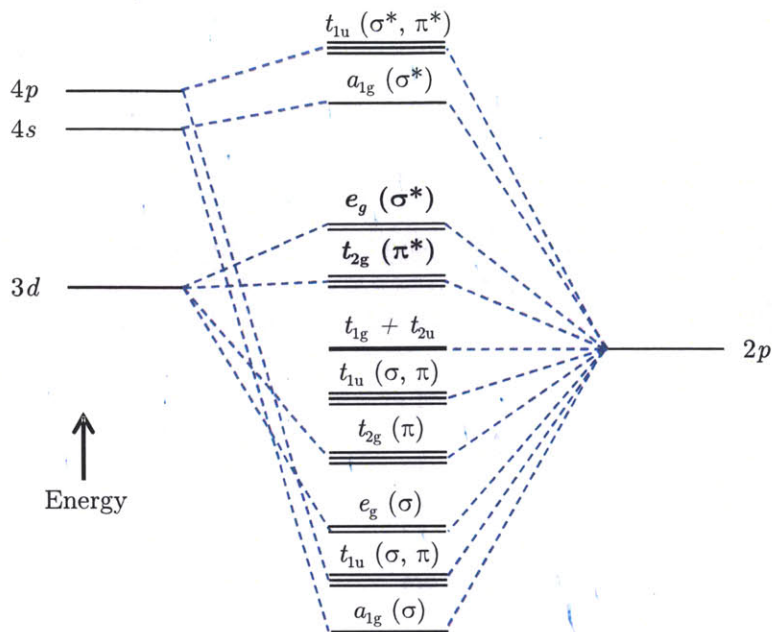


Figure 1.3: Qualitative molecular orbital diagram for octahedrally-coordinated transition metal ion. Asterisks denote antibonding states. In bold are the e_g and t_{2g} states of interest in catalysis. Figure adapted from Cox.⁷⁸

Numerous perovskite oxides were studied in the early 1980s by Bockris and coworkers,^{72,73} as well as Matsumoto et al.⁷⁹⁻⁸³ Several possible mechanistic pathways⁷³ were proposed, attempts were made to correlate the catalytic activity with M-OH bond strength and number of d -electrons, and the possible importance of different orbital occupancies was mentioned.⁷² Nickel and cobalt perovskites were typically regarded as the most active perovskites for oxygen evolution.^{75,79} More recently, a scheme was proposed based on a simplified molecular orbital model that uses the e_g orbital occupancy as a descriptor for perovskite OER activity,¹⁰ similarly to the case for the oxygen reduction reaction,⁷⁶ which was itself inspired by the d -band center theory for metal surfaces.^{84,85} The OER activities of a series of perovskites were found to form a volcano plot (Figure 1.4) when plotted versus the e_g orbital filling, which was determined via X-ray absorption near edge structure (XANES) and spin states inferred

from other studies in the literature. Perovskites with an e_g orbital occupancy of approximately 1 were found to be the most active (e.g. LaNiO_3 , LaCoO_3) and based on this principle a highly active perovskite catalyst, $\text{Ba}_{0.5}\text{Sr}_{0.5}\text{Co}_{0.8}\text{Fe}_{0.2}\text{O}_{3-\delta}$ was discovered, showing that these descriptors can be used to rationally choose materials as candidates for promising OER catalysts. From this work, this thesis has extended the study of some perovskite catalysts, studying further the catalytic activity and surface structure changes that occur on $\text{Ba}_{0.5}\text{Sr}_{0.5}\text{Co}_{0.8}\text{Fe}_{0.2}\text{O}_{3-\delta}$ and related compounds.

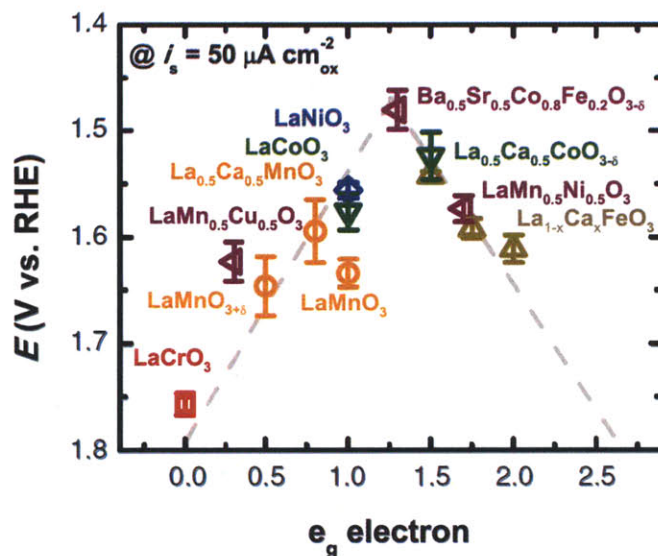


Figure 1.4: Volcano plot showing the relationship between OER catalytic activity, defined as the overpotential at $50 \mu\text{A cm}^{-2}$ (estimated true oxide surface area), and the e_g orbital occupancy of the B-site transition metal ion. Figure from previous work.¹⁰

1.4 Scope of this Thesis

This thesis presents an investigation of the surfaces of perovskite oxide catalysts before and after electrochemical measurements in alkaline electrolyte. The highly active catalyst BSCF82 was observed to have unusual pseudocapacitance relative to other perovskites studied.¹⁰ Further investigation of the electrochemical behavior of this

catalyst and other perovskites is presented. Then, high resolution transmission electron microscopy (HRTEM) shows that BSCF82 and the closely related compounds $\text{SrCo}_{0.8}\text{Fe}_{0.2}\text{O}_{3-\delta}$ (SCF82) and $\text{Ba}_{0.5}\text{Sr}_{0.5}\text{Co}_{0.4}\text{Fe}_{0.6}\text{O}_{3-\delta}$ (BSCF46) undergo a structural change (distinct from corrosion) at their surfaces to an amorphous oxide. This surface change is concomitant with an increase in the pseudocapacitive current and the OER activity. The other perovskite catalysts were investigated that remained crystalline under identical conditions. Raman spectroscopy is shown to be an effective tool for quickly determining whether an oxide rapidly becomes amorphous at the surface during OER. The effects of different electrochemical conditions, such as cycling electrodes or holding potentiostatically, and changing the potential window, are also discussed. Parallels between the amorphous surface layers and electrochemically-deposited cobalt oxide film catalysts are drawn. Based on density functional theory calculations, it is shown that the calculated oxygen p -band center position relative to the Fermi level is a descriptor for both experimental OER activity and stability in the perovskites studied. Finally, further interpretations and hypotheses based on the data are discussed along with future research directions. This work illustrates the importance of understanding the exact nature of the oxide surface where the OER takes place, in order to further understand and develop active and stable oxide catalysts for the OER.

2 Experimental

2.1 Oxide Synthesis and Characterization

Several techniques were utilized in this study for synthesizing perovskite oxides, including LaCoO_3 (LCO), LaMnO_3 (LMO), $\text{La}_{0.4}\text{Sr}_{0.6}\text{CoO}_{3-\delta}$ (LSC46), $\text{SrCo}_{0.8}\text{Fe}_{0.2}\text{O}_{3-\delta}$ (SCF82), and $\text{Ba}_{0.5}\text{Sr}_{0.5}\text{Co}_{1-y}\text{Fe}_y\text{O}_{3-\delta}$ ($y = 0.2, 0.6$; BSCF82 and BSCF 46, respectively). For LCO and LMO a co-precipitation method was used, where metal nitrates (99.98%, Alfa Aesar) were mixed in the desired molar ratio in deionized water (18 M Ω -cm, Millipore) such that metal concentrations were approximately 0.1 M. This solution was titrated with 1.2 M tetramethylammonium hydroxide (100%, Alfa Aesar) until a precipitate formed. This precipitate was then filtered and dried before annealing at 1000° C. LCO was annealed in dry air, while LMO was annealed in Ar.

BSCF82 and BSCF46 were synthesized by a nitrate combustion method.¹⁰ The alkaline earth and transition metal nitrates (99.9998+%, Sigma-Aldrich) were added in the desired molar ratio to deionized water at approximately 0.2 M concentration. The mixture was then heated until most of the water had evaporated, and continued until sparks were observed in the remaining powder, indicating combustion of the nitrates. After the sparking had ceased, the powder was annealed in air at 1100° C for 24 h.

SCF82 was synthesized by solid-state reaction. SrCO_3 , Co_3O_4 , and Fe_2O_3 were mixed in the correct molar ratio, ground with a mortar and pestle and fired in air at 1000° C for 12 h. The powder was then ground again and annealed in air at 1100° C for 24 h with intermediate grindings.

LSC46 was synthesized by the Pechini method.⁸⁶ Similarly to the above methods, metal nitrates were measured out in the desired molar ratio and added to deionized water. Citric acid (99%, Sigma-Aldrich) was added in a 5:1 molar ratio of citric acid to total metal cations. The mixture was stirred at 75° C for 30 min, before adding ethylene glycol in a 1:1 molar ratio to citric acid. This mixture was covered and stirred at 90° C for 1 h.

Phase purity was verified via X-ray diffraction with a Rigaku high-power rotating anode X-ray powder diffractometer with a typical range of 30° to 95° 2 θ under Cr K $_{\alpha}$ radiation. All oxides used in this study showed no sign of impurity phases.

Particle size analysis was performed using scanning electron microscopy (SEM, JEOL 6320 FV). Specific area (cm²/mg) was calculated using a spherical geometry approximation:⁸⁷

$$A_S \approx \frac{\sum \pi d^2}{\sum (\frac{1}{6}) \rho \pi d^3} = \frac{6 \sum d^2}{\rho \sum d^3} = \frac{6}{\rho d_{r/a}} \quad (2.1)$$

Each sum was calculated over all the individual particles counted in the micrographs. Adobe Photoshop CS5 was used to select particles using the lasso tool, and the image analysis tools were used to obtain two-dimensional areas for each selected particle, from which an effective spherical diameter was obtained for use in equation 2.1. Powder specific areas determined via this method have been found to agree fairly well with those obtained by Brunauer, Emmet and Teller (BET) analysis, typically within a factor of 2-3.^{10,88}

2.2 Electrode Preparation

Electrodes were prepared by a catalyst ink drop-casting technique.⁸⁸ Catalyst ink was prepared by weighing out oxide power and acetylene black (AB) carbon in a 5:1 weight ratio and dispersing in tetrahydrofuran (THF, 99%, Sigma-Aldrich) such that 10 μL of solution contained 0.05 mg of oxide. This dispersion was bath-sonicated for 1 h, and tip-sonicated for 10 min before adding KOH-neutralized Nafion[®] polymer (DE520, Ion Power, DE) as binder in a 1:1 weight ratio to AB carbon and bath sonicating again for 2 min. The Nafion solution was prepared by dropping in 0.1 M KOH to the as-purchased Nafion liquid, with a 2:1 volume ratio of Nafion to KOH. Then, 10 μL of ink was deposited on a glassy carbon rotating disk electrode with a micro-pipette such that oxide loading was 0.25 mg/cm^2 and left to dry. Electrodes that were prepared for Raman spectroscopy measurements did not contain AB carbon in order to avoid background signal.

2.3 Electrochemical Measurements

Electrochemical experiments were conducted using a rotating disk electrode setup consisting of a borosilicate glass cell, either a saturated calomel reference electrode (SCE) or Ag/AgCl reference electrode, platinum wire counter electrode and Teflon electrode holder (all from Pine Instruments) and a Biologic SP-300 potentiostat. Reference electrodes were calibrated in 0.1 M KOH by bubbling hydrogen gas (ultra-high purity, Airgas) for 20 minutes and measuring hydrogen oxidation/evolution at a platinum disk electrode. The open-circuit potential was then defined as 0 V versus reversible hydrogen electrode (RHE) after verifying stable, reversible electrochemical

behavior. The electrolyte prepared with deionized water ($> 18 \text{ M}\Omega\cdot\text{cm}$, Millipore) and KOH pellets (99.99% purity metals-basis, Sigma-Aldrich) to yield a concentration of 0.1 M. For OER measurements, oxygen gas (ultra-high purity, Airgas) was bubbled for 15-20 minutes before electrochemical measurements, and was continued during measurements, to ensure $\text{O}_2/\text{H}_2\text{O}$ equilibrium at 1.23 V versus RHE. Cyclic voltammetry measurements used a scan rate of 10 mV/s. All measurements used a rotation rate of 1600 rpm, with the exception of electrodes prepared for Raman spectroscopy, which used a rotation rate of 900 rpm. There was no observed dependence of OER current on rotation rate in the potential windows accessed in this study. High-frequency AC impedance was used to determine the ohmic resistance R of the electrolyte (typically 45Ω for 0.1 M KOH). Ohmic losses were corrected by subtracting the ohmic drop iR from the measured potential where i is the measured current and R is the electrolyte resistance as described above. Potentials corrected for ohmic drop are denoted as $E - iR$. OER kinetic currents were capacitance-corrected by taking the average between positive- and negative-going scans, and the specific activity was obtained by normalizing the current by the surface area of each oxide as estimated via SEM measurements described previously.

2.4 Characterization of Electrochemically-Cycled Electrodes

Samples were prepared for transmission electron microscopy (TEM) by removing the electrode from electrolyte following electrochemical measurements, rinsing briefly with ethanol, then swabbing a lacy carbon grid over the electrode. Grids were dried and

stored in a vacuum oven at 70° C. Samples of the as-synthesized powders were made by sonicating the powder in THF for 5 minutes and then collecting the powder on a lacy carbon grid, followed by drying in a vacuum oven at 70° C.

TEM was conducted on a JEOL 2010F instrument operated at 200 keV. The microscope was equipped with a field-emission electron gun and ultra-high resolution pole piece, yielding a point-to-point resolution of 1.9 Å. Fourier image analysis was performed using Gatan Digital Micrograph software v2.01 (Gatan).

Energy-dispersive X-ray spectroscopy (EDS) was performed by operating the TEM in scanning mode using an electron beam of approximately 0.7 nm. INCA (Oxford Instruments) software was used for controlling beam position and for data analysis. Live acquisition time was 60 s for each EDS spectrum, with the beam placed at various positions on the catalyst surface or bulk, with a spatial resolution of approximately 2 nm owing to sample drift during data acquisition.

Raman spectroscopy performed on electrodes after electrochemical measurements was done by removing the electrode from electrolyte, drying with compressed air and using the electrode directly under the microscope of the LabRAM HR800 (Horiba Jobin Yvon). A 633 nm He/Ne laser at 0.2 or 2 mW was used with a 50× objective (giving spot size of approximately 30 μm^2), at room temperature. Sampling time was adjusted per sample to yield approximately the same signal-to-noise ratio for each measurement (6×30 s for LMO, 6×60 s for LCO, 6×60 s for BSCF82 (0.7-1.0 V potential range), 3×120 s for BSCF82 (all other potential ranges), and 6×120 s for LSC46). No change in the Raman peak intensity was observed over the course of the 3-12 min sampling time. Spectra were collected at six or more locations on each electrode.

2.5 Density Functional Theory Calculations

Density functional theory (DFT) calculations used the Vienna ab initio simulation package (VASP) with the Project-Augmented plane-wave method.⁸⁹⁻⁹¹ Exchange-correlation was treated with the Perdew-Wang-91 generalized gradient approximation (GGA) with soft O_s oxygen pseudopotential and the Hubbard U correction.^{92,93} Energy convergence was within 3 meV per perovskite formula unit from a Monkhorst-Pack $4 \times 4 \times 4$ k -point mesh. The calculations are performed using the simplified spherically averaged approach,⁹⁴ where U_{eff} is applied to d electrons ($U_{eff} = U_{coulomb} - \text{exchange } J$) with values of 4, 4, and 3.3 eV for Mn, Fe, and Co, respectively.^{95,96} Typically, $2 \times 2 \times 2$ perovskite supercells were used for simulations and fully stoichiometric compounds were used (no oxygen vacancies). For perovskites with disordered cations (i.e. BSCF46, BSCF82, SCF82 and LSC46) a special quasirandom structure (SQS) approach was used.⁹⁷ Several sampled configurations' calculated O p -band centers were used in a weighted average (weighted by the Boltzmann factor at 300 K for the energy of the sampled configurations) to achieve an effective O p -band center.

3 Results and Discussion

3.1 Material Characterization

X-Ray diffraction (XRD) was performed on all oxides, namely LaCoO_3 (LCO), LaMnO_3 (LMO), $\text{La}_{0.4}\text{Sr}_{0.6}\text{CoO}_{3-\delta}$ (LSC46), $\text{SrCo}_{0.8}\text{Fe}_{0.2}\text{O}_{3-\delta}$ (SCF82), and $\text{Ba}_{0.5}\text{Sr}_{0.5}\text{Co}_{1-y}\text{Fe}_y\text{O}_{3-\delta}$ ($y = 0.2, 0.6$; BSCF82 and BSCF 46, respectively), to ensure phase purity. The resulting diffractometry results are shown in Figure 3.1, with relevant extracted lattice parameters summarized in Table 3.1. All XRD data was gathered from pure oxide powder with the exception of LSC46, which included Si as a reference (Figure 3.2).

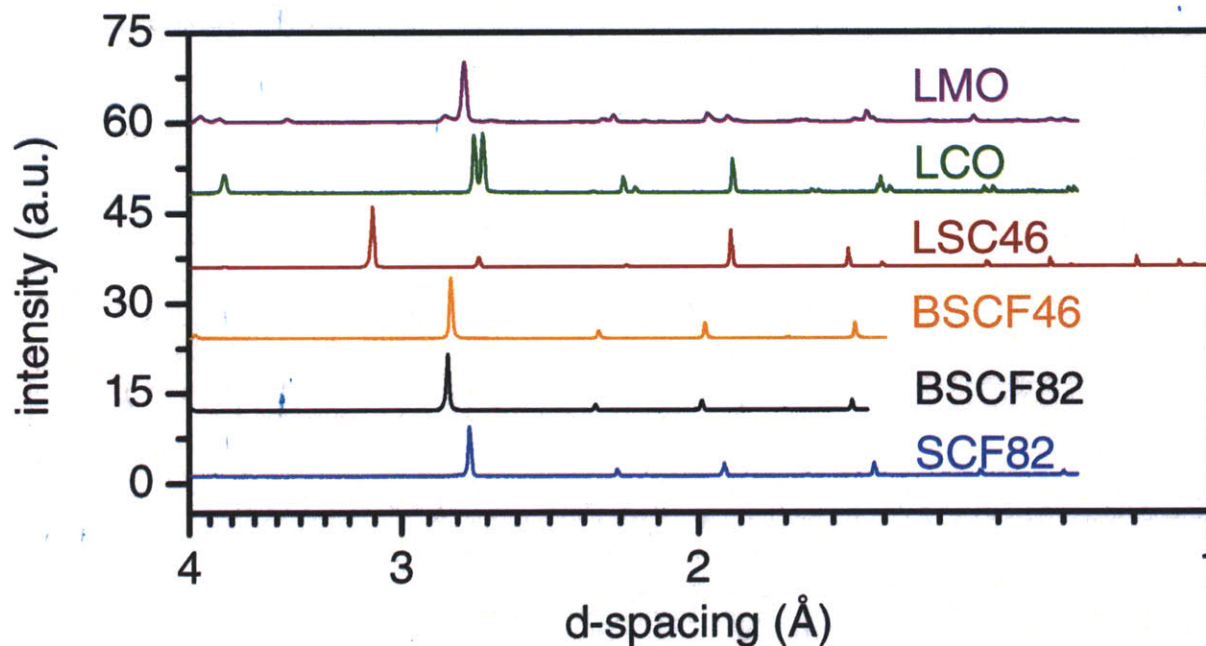


Figure 3.1: X-ray diffraction data for the oxides studied in this work. LMO, LCO data were gathered by Jin Suntivich. LSC46 data were gathered by Ethan J. Crumlin. SCF82 data were gathered by Alexis Grimaud.

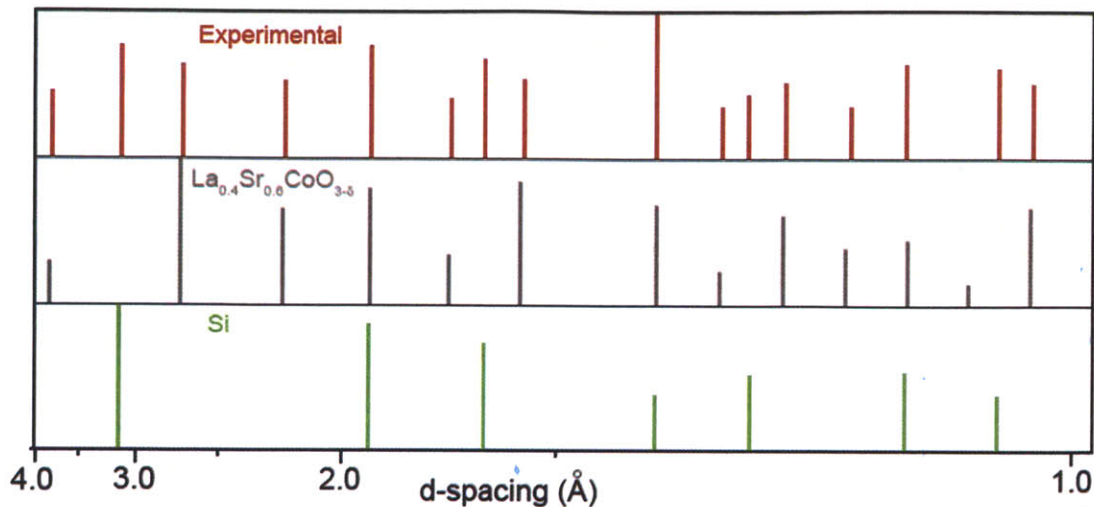


Figure 3.2: Experimental XRD peak locations (red) with database peak positions for LSC46 (gray) and Si (green). Si was included to give reference diffraction peaks.

Table 3.1: Space groups and lattice parameters of the oxides studied in this work.

Material	Space Group	Lattice Parameters (Å)		
		a	b	c
LMO	Pnma	5.66	7.22	5.53
LCO	R $\bar{3}c$	5.44	5.44	13.09
LSC46	Pm $\bar{3}m$	3.84	3.84	3.84
BSCF46	Pm $\bar{3}m$	3.96	3.96	3.96
SCF82	Pm $\bar{3}m$	3.86	3.86	3.86
BSCF82	Pm $\bar{3}m$	3.99	3.99	3.99

Oxide surface area estimations were calculated based on scanning electron microscopy (SEM; see Chapter 2.1). Calculated values of A_s are tabulated in Table 3.2.

Table 3.2: SEM-estimated surface areas of oxides in this work.

Material	Specific Area (m ² ·g ⁻¹)
LMO	0.6
LCO	0.7
LSC46	1.2
BSCF46	0.1
SCF82	0.1
BSCF82	0.2

3.2 Electrochemical Measurements

Cyclic voltammetry was performed on LCO, LMO, LSC46, SCF82, BSCF46 and BSCF82, with the 1st and 5th cycles shown in Figure 3.3. The OER activity, defined as the overpotential required for a given current density normalized to true oxide surface area, increases as expected,¹⁰ with $LMO < LCO < LSC46 \approx BSCF46 < SCF82 \approx BSCF82$. The cyclic voltammograms of LCO, LMO, and LSC46 all reached a steady-state after the first five cycles, after which no significant changes in the OER activity were observed. In contrast, BSCF82 exhibited a drastic change in both pseudocapacitive current and OER activity. OER activity increased steadily with cycling up to around the 50 cycle mark (Figure 3.4a), after which it reached a steady-state with approximately 4 times greater OER current at 1.6 V versus reversible hydrogen electrode (RHE) than that of the first cycle. In contrast, LSC46 cycled up to 100 times did not undergo any significant changes in OER behavior (Figure 3.4b).

Potentiostatic measurements were performed to observe any changes versus time, and also to verify that the cyclic voltammetry measurement with the appropriate data analysis yielded accurate values for the OER activity. Figure 3.4c shows potentiostatic measurements at four applied potentials, on separate electrodes from those used for cyclic voltammetry. In Figure 3.4d, any discrepancy between the potentiostatic (solid marker) and cyclic voltammetry data (hollow marker) is explained by the experimental error in the electrode deposition and not by the technique used, as seen in Figure 3.5.

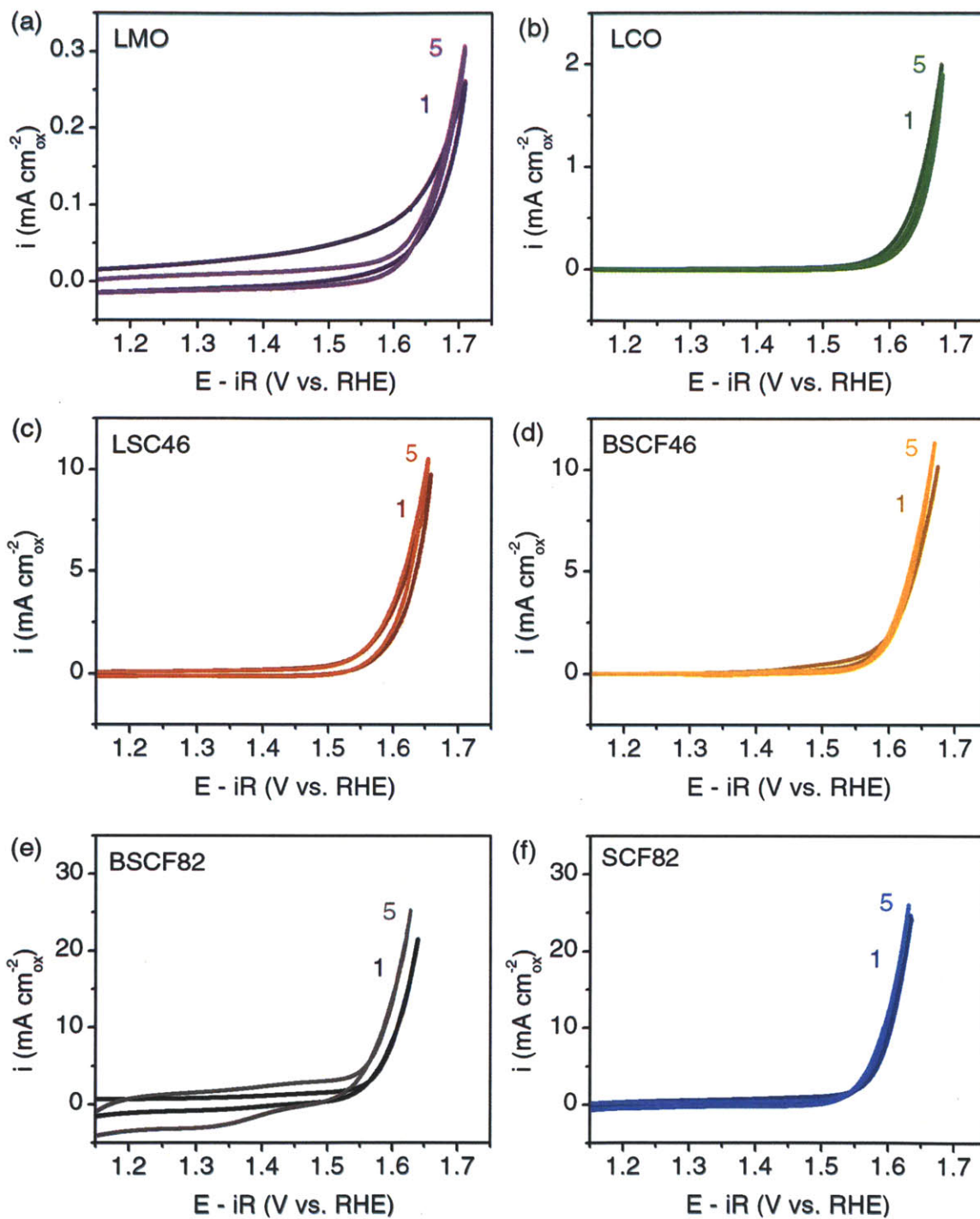


Figure 3.3: Cyclic voltammetry for (a) LMO, (b) LCO, (c) LSC46, (d) BSCF46, (e) BSCF82 and (f) SCF82. Number labels n indicate the n^{th} cycle of cyclic voltammetry (1.1-1.7 V versus RHE, 10 mV/s). All measurements were performed in O₂-saturated 0.1 M KOH, corrected for ohmic losses and normalized to the SEM-estimated surface area of oxides, and used an oxide loading of 0.25 mg/cm² supported on glassy carbon. Figure adapted from published work.¹¹

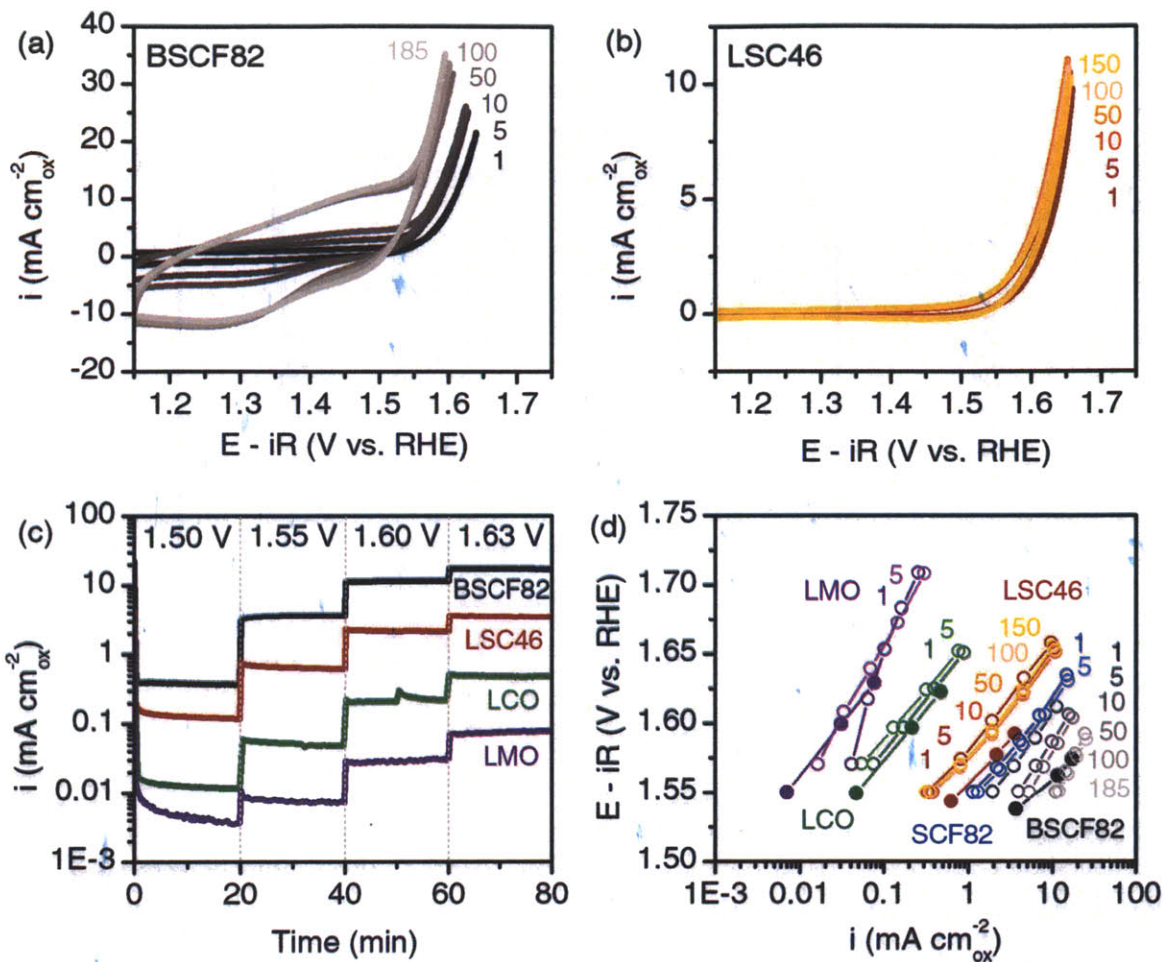


Figure 3.4: Heavy cycling of (a) BSCF82 and (b) LSC46; (c) Potentiostatic measurements on BSCF82, LSC46, LCO and LMO; (d) Tafel plot containing cyclic voltammetry at the n^{th} cycles (hollow markers) and potentiostatic data (solid markers) for comparison. Figure adapted from published work.¹¹

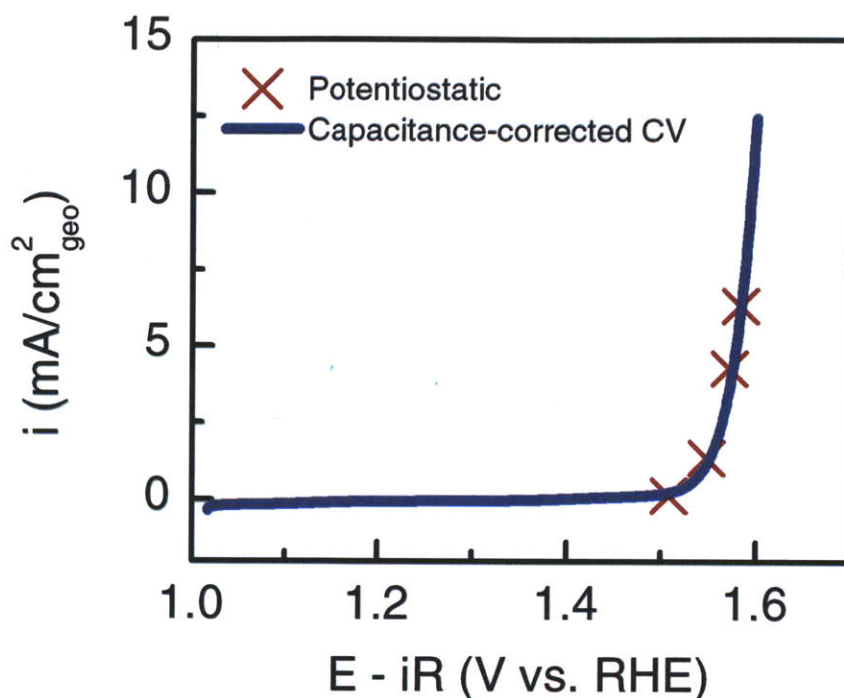


Figure 3.5: Capacitance- and ohmic-corrected cyclic voltammogram data (1.0-1.7 V versus RHE, 10 mV/s) of a BSCF82 electrode (0.25 mg/cm² oxide loading) on the first cycle (blue line). Also shown are potentiostatic data on the same electrode taken immediately after the first cycle (red X). Measurements taken in O₂-saturated 0.1 M KOH, normalized to geometric electrode area. Figure adapted from published work.¹¹

In verifying that the current observed is attributable to OER, we first note that it has previously been observed from rotating ring-disk experiments that current in this potential range is indeed almost 100% OER.¹⁰ To rule out corrosion or oxidation of cobalt/iron in BSCF82 as being significant contributions to the observed current, the ratio of electrons passed during the observed oxidation current to the total number of cobalt and iron atoms present in BSCF82 was calculated. To obtain the total charge passed that is attributable to OER, the capacitance- and iR-corrected current was integrated (using the data from Figure 3.4a). To include current from both forward and backward scans, the average of the forward and backward scans was mirrored in time

for each cycle, as seen in Figure 3.6. Using this method, the ratio of electrons passed to total cobalt and iron atoms is over 100 for both cyclic voltammetry and potentiostatic/chronoamperometric (Figure 3.7) measurements. The ratio of oxygen evolved to total oxygen present in the BSCF82, also calculated from amount of Faradaic charge transfer, is approximately 10 for both cyclic voltammetry and potentiostatic measurements. Because the catalytic activity was not observed to decrease during the course of any experiments, dissolution or corrosion current is negligible when compared with the OER current.

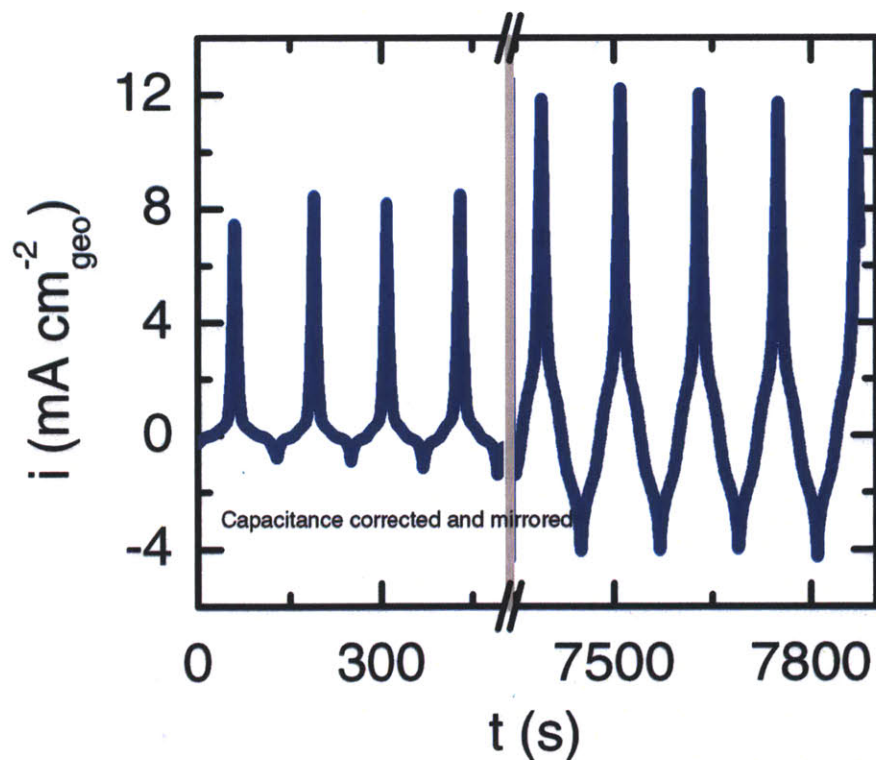


Figure 3.6: Selected regions of the data shown in Figure 3.4a. Data are capacitance- and iR -corrected. For each cycle, the average of the forward and backward scan was mirrored in time to account for current from both forward and backward scans. Figure adapted from published work.¹¹

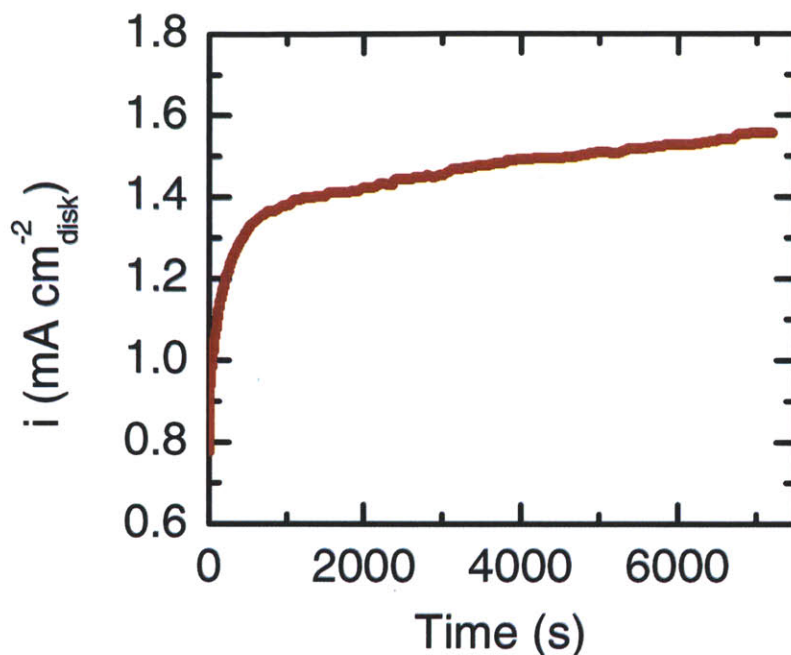


Figure 3.7: Potentiostatic data measured on a single BSCF82 electrode, held at 1.6 V vs. RHE for 2 h. This electrode did not contain AB carbon. Measurement performed by Marcel Risch. Figure adapted from published work.¹¹

3.3 Transmission Electron Microscopy

High-resolution transmission electron microscopy (HRTEM) was used to examine the surfaces both as-prepared powder and electrodes that had been cycled five times from 1.1 to 1.7 V versus RHE. The surfaces of the as-prepared oxide powders were highly crystalline; the surfaces of BSCF82 had very few thin amorphous regions. The fast Fourier transforms (FFTs) of all the HRTEM images of the as-prepared particle surfaces can all be indexed to the bulk crystal structure of the corresponding oxide (Figure 3.8). After cycling, amorphous regions around 10 nm thick were present on the surfaces of BSCF82, SCF82 and BSCF46. For BSCF82 cycled 185 times, the particles became amorphous to the extent that could be observed with HRTEM (Figure 3.9c).

HRTEM was performed on electrodes with and without AB carbon, with no significant differences between the two (Figure 3.10). In contrast, the surfaces of LMO, LCO and LSC46 remained crystalline after cycling, comparable to the as-prepared samples (Figure 3.8c-h). This does preclude instability in longer time scales or different voltage regimes.

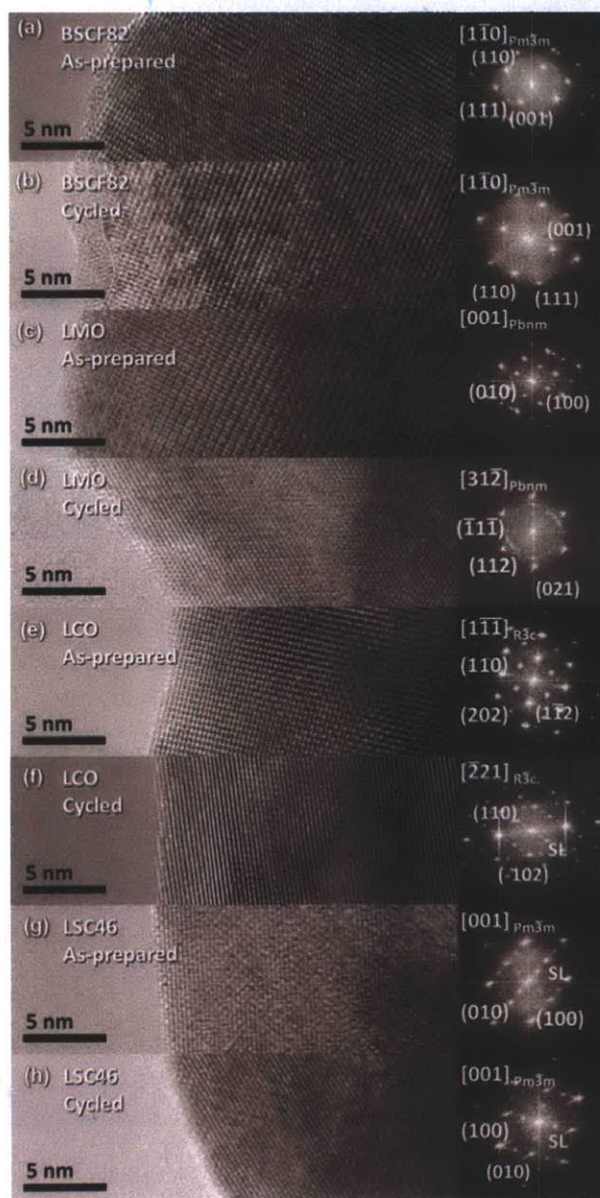


Figure 3.8: HRTEM and FFTs from approximately 35×35 nm areas of (a) as-prepared BSCF82, (b) cycled BSCF82, (c) as-prepared LMO, (d) cycled LMO, (e) as-prepared LCO, (f) cycled LCO, (g) as-prepared LSC46 and (h) cycled LSC46. Cycling consisted of five cycles between 1.1-1.7 V vs. RHE in O_2 -saturated 0.1 M KOH at 10 mV/s. HRTEM performed by Christopher E. Carlton. Figure adapted from published work.¹¹

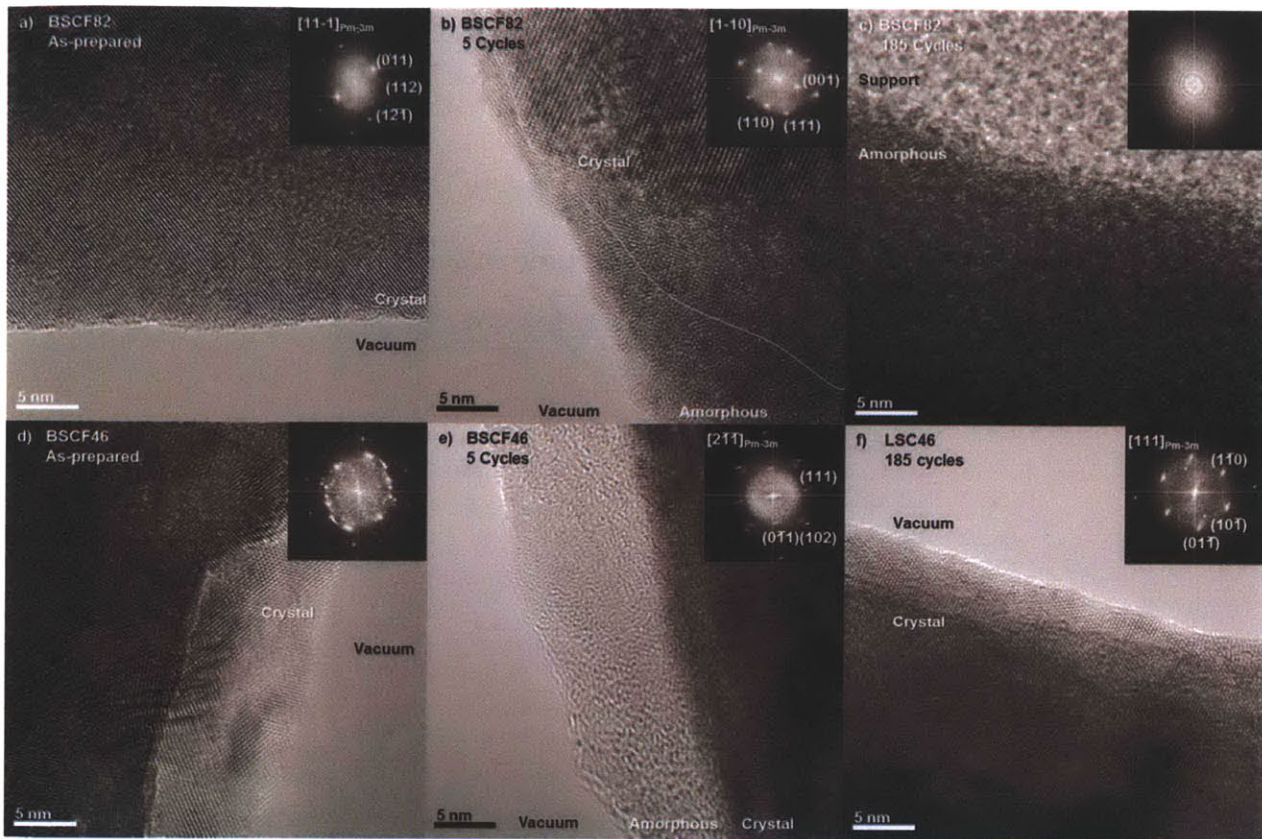


Figure 3.9: HRTEM and FFTs of (a) as-prepared BSCF82 powder, (b) BSCF82 cycled 5 times, (c) BSCF82 cycled 185 times, (d) as-prepared BSCF46, (e) BSCF46 cycled 5 times, and (f) LSC46 cycled 185 times. Cycles were 1.1-1.7 V vs. RHE at 10 mV/s, in O₂-saturated 0.1 M KOH. HRTEM performed by Christopher E. Carlton. Figure adapted from published work.¹¹



Figure 3.10: HRTEM and FFT of BSCF82 electrode that was cycled 5 times (a) with AB carbon and (b) without AB carbon. The amorphous layers are similar and show that AB carbon does not significantly contribute to the amorphization process. HRTEM performed by Christopher E. Carlton. Figure adapted from published work.¹¹

Analysis of the FFT patterns from HRTEM images collected from the surface amorphous regions of BSCF82 revealed a bright diffuse ring that corresponds to a spacing of approximately 2.8 Å in real space (Figure 3.11b-c). This spacing, which is not present in the interatomic distances of cubic perovskite (containing only corner-shared transition metal octahedra), matches the cobalt/iron spacing in edge-sharing octahedra.^{98,99} Energy-dispersive X-ray spectroscopy (EDS) performed in the surface amorphous regions of BSCF82 revealed a decrease in the concentrations of the A-site cations Ba²⁺ and Sr²⁺, which suggests A-site cation leaching during cycling (Figure 3.12).

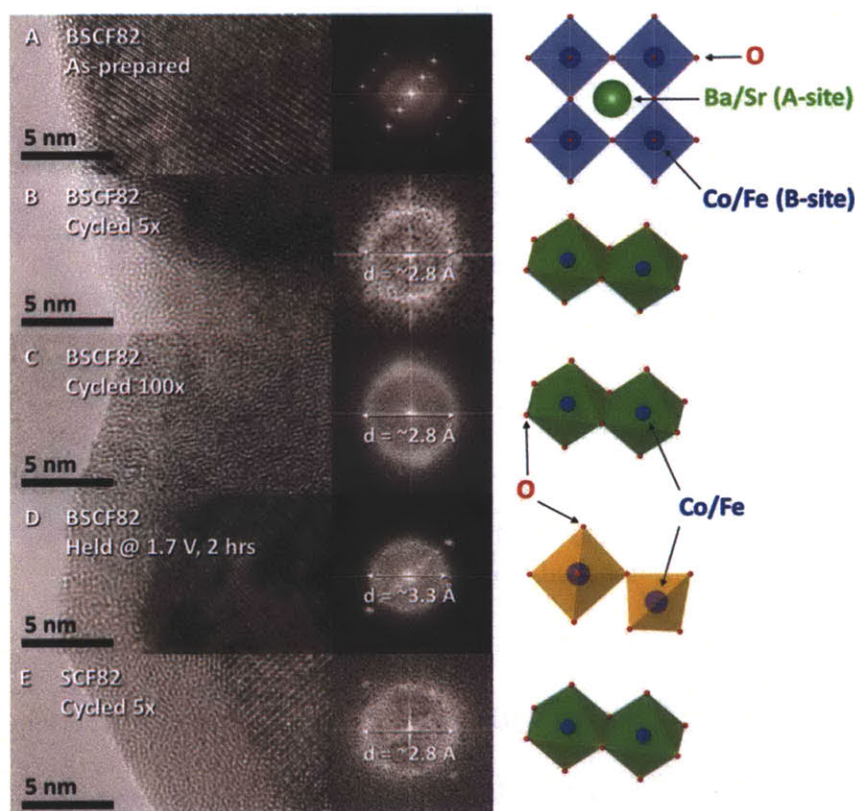


Figure 3.11: HRTEM and corresponding FFTs of particle surfaces of (a) as-prepared BSCF82, (b) BSCF82 cycled 5 times, (c) BSCF82 cycled 100 times, (d) BSCF82 held potentiostatically at 1.7 V vs. RHE for 2 h, and (e) SCF82 cycled 5 times. Cycles were 1.1-1.7 V vs. RHE at 10 mV/s, in O₂-saturated 0.1 M KOH. HRTEM performed by Christopher E. Carlton. Figure adapted from published work.¹¹

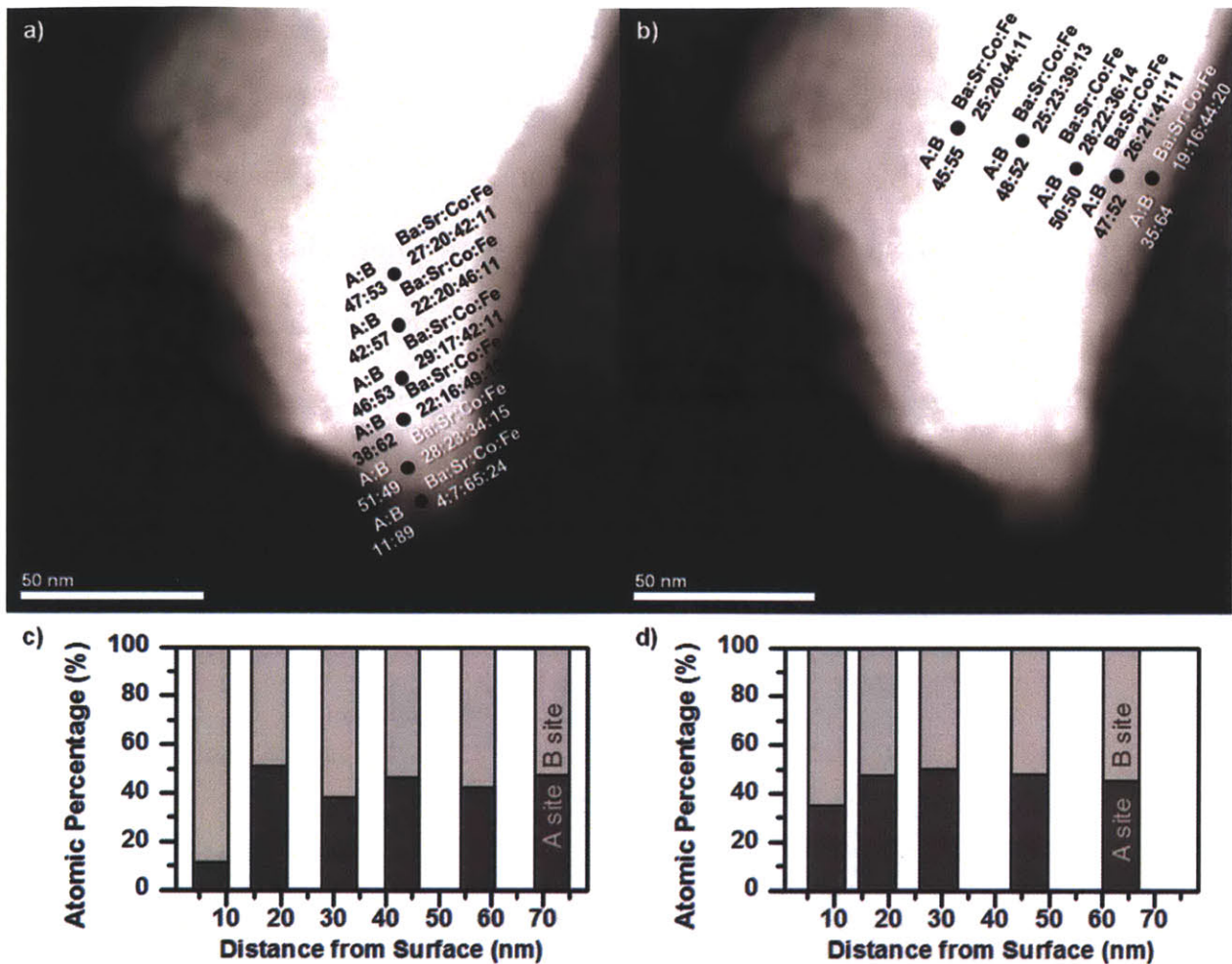


Figure 3.12: High angular annular dark field imaging and scanning TEM EDS of BSCF82 cycled 5 times between 1.1-1.7 V vs. RHE at 10 mV/s, in O₂-saturated 0.1 M KOH. The quantitative EDS results are shown in both the images (a) and (b), and plotted vs. the distance from the particle edge in (c) and (d). Both (a) and (b) are the same image, with EDS taken at different locations on the particle. A-site atom concentration (Ba and Sr) is compared to B-site concentration (Co and Fe) for visual clarity. HRTEM/EDS performed by Christopher E. Carlton. Figure adapted from published work.¹¹

Amorphous regions were also found in BSCF82 electrodes that were held potentiostatically at 1.7 V versus RHE for 2 h (Figure 3.11d). Although the total amount of charge passed was much higher during this experiment than in the case of cycling 5 times, the thickness of these regions was comparable to the 5× cycled case. Interestingly, this suggests that cycling the potential dramatically increases the rate of

the amorphization process. Also, in the FFT of the HRTEM images of the potentiostatically held electrode, a diffuse ring with real space spacing of approximately 3.3 Å was observed, which corresponds to interatomic distance of cations in spinel Co_3O_4 . This could indicate the formation of spinel-like motifs containing both octahedral and tetrahedral environments for cobalt and iron cations, as reported for BSCF82 at intermediate temperatures.¹⁰⁰ The existence of spinel-like motifs is further supported by Raman spectroscopy, where approximately 15% of all spectra contained peaks similar to those present in spinel Co_3O_4 (Figure 3.13).

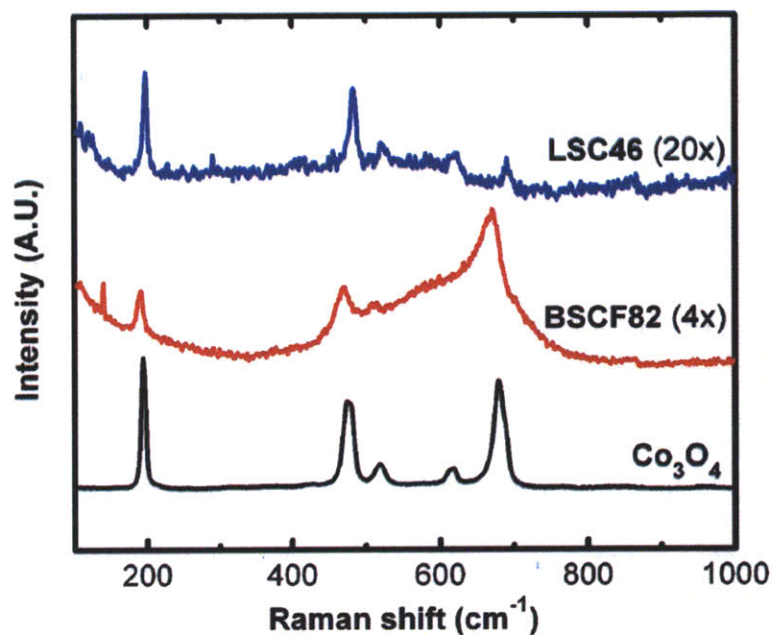


Figure 3.13: Co_3O_4 peaks have been observed in the Raman spectra of both BSCF82 and LSC46, both cycled 5 times between 1.1-1.7 V vs. RHE at 10 mV/s. The multipliers in the image refer to intensity scaling for visual clarity. Approximately 15% of spectra exhibited the Co_3O_4 -like peaks. These peaks were never observed for as-prepared samples or in LCO samples before or after cycling. Raman spectroscopy performed by Kelsey A. Stoerzinger. Figure adapted from published work.¹¹

3.4 Raman Spectroscopy and Potential-Dependent Amorphization

Raman spectroscopy can be used as a rapid tool for probing the amorphization of oxide surfaces after it has been established (e.g. via HRTEM) that such a process occurs, and the oxides in question are Raman active. The Raman spectra of BSCF82 prior to cycling exhibits a broad peak at around 675 cm^{-1} , attributed to internal motion of oxygen within the cobalt and iron octahedra.¹⁰¹ It is of interest to investigate the conditions under which amorphization occurs, by varying the potential window used. When BSCF82 was cycled between 1.1 and 1.7 V versus RHE as in the electrodes examined via HRTEM, the vibrational mode of BSCF82 mentioned above broadens after 5 cycles and was absent after 50 cycles. This is in good agreement with the changes in the electrochemical data and the amorphization observed via HRTEM. Since the information depth of Raman spectroscopy is estimated to be larger than 100 nm, the lack of Raman signal after 50 cycles indicates that the amorphous layer is likely larger than 100 nm, beyond the thicknesses that can be observed with HRTEM (approximately 20 nm). In contrast, the Raman spectra for LMO, LCO and LSC46 (Figure 3.14) have negligible changes after cycling. Of particular interest are the peaks at 420 and 600 cm^{-1} for LCO, which have been attributed to bending and breathing modes of the oxygen cage of E_g and A_{2g} symmetry, respectively.¹⁰² These peaks remained visible after 50 cycles (Figure 3.14b), showing that there is no significant change in the local symmetry of LCO when cycled under identical conditions to those of BSCF82.

The effect of changing the cyclic voltammetry window was investigated by cycling BSCF82 50 times (at 10 mV/s) in three voltage ranges: $0.7\text{-}1.0\text{ V}$, $1.1\text{-}1.5\text{ V}$, and

1.5-1.7 V versus RHE. No significant changes to the Raman spectra were observed for the 0.7-1.0 V and 1.1-1.5 V voltage ranges; the 1.5-1.7 V range, showed loss of Raman scattering accompanying the formation of a thick amorphous layer (Figure 3.14c). This suggests that amorphization is potential-dependent and occurs most rapidly at potentials above 1.5 V vs. RHE, where OER current is appreciable.

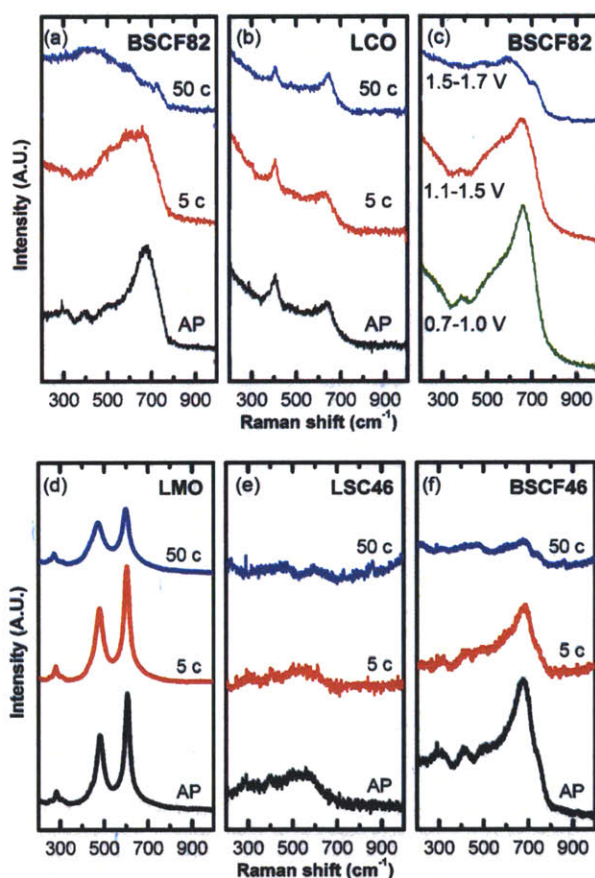


Figure 3.14: Raman spectra of (a) BSCF82 and (b) LCO before and after cycling 5 and 50 times, (c) BSCF82 after cycling 50 times in the indicated voltage windows, (d) LMO, (e) LSC46 and (f) BSCF46 before and after cycling 5 and 50 times. Cycling took place in O_2 -saturated 0.1 M KOH at 10 mV/s. Raman spectroscopy performed by Kelsey A. Stoerzinger. Figure adapted from published work.¹¹

Various potentiostatic conditions were also investigated, comparing different voltages with a fixed amount of charge passed. Similarly to the BSCF82 after cycling, reduction of Raman scattering was observed at OER potentials (Figure 3.15). Oxidation

current was also seen to increase over time; only when potential was held in the OER region. At 1.45 V versus RHE for 24 h, no strong decrease in Raman signal was observed, indicating that any amorphization layer is extremely small. OER potential ranges may be essential for the rapid amorphization observed in BSCF82 and closely related perovskites. Thus it is possible that OER may kinetically permit or enhance the amorphization process, although this requires further investigation.

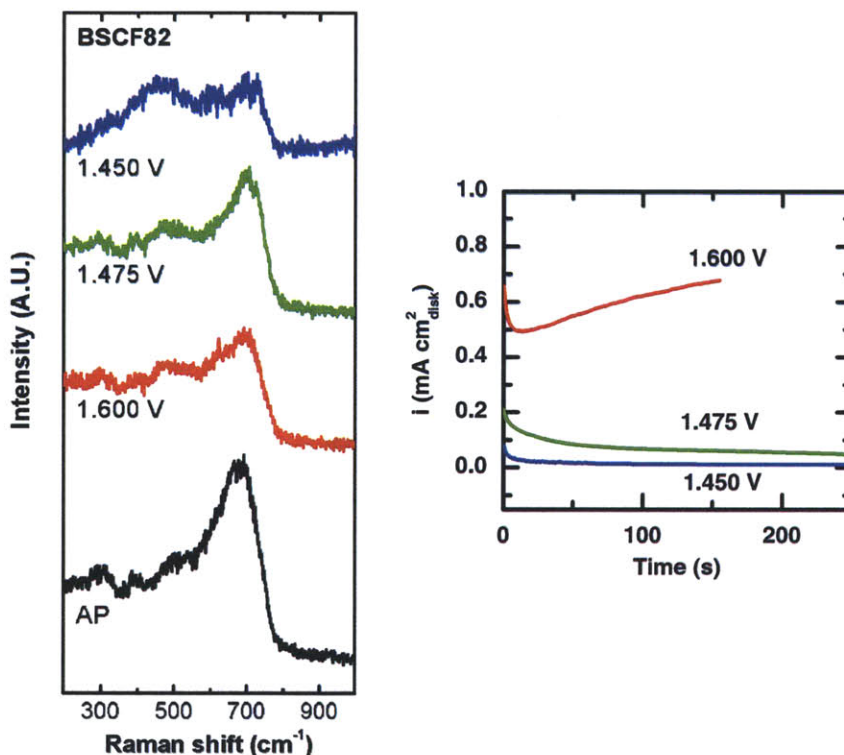


Figure 3.15: Raman spectra (left) of BSCF82 after potentiostatically holding at the labeled potential until 27.4 mC of charge had passed. Electrochemical data is shown on the right panel. Times required were 0.06, 1.78, and 24 h for 1.600 (red), 1.475 (green) and 1.45 (blue) V vs. RHE, respectively. For potentials with appreciable OER current, the current increased over time, accompanying more drastic changes in the Raman spectra. Raman spectroscopy performed by Kelsey A. Stoerzinger. Figure adapted from published work.¹¹

3.5 Amorphization and Pseudocapacitive Current

The simultaneous increase in pseudocapacitive current, OER current, and amorphous layer thickness leads to the possibility that the amorphous regions may be accessible to electrolyte.^{103 105} This would potentially increase the effective number of active sites for OER, and would also allow redox of the B-site cations to occur in the bulk of the material, possibly explaining the change in pseudocapacitive current. A rough measure of the electrochemically active surface area was performed by determining the cathodic charge passed during the negative-going scan of cyclic voltammetry, which would be proportional to the pseudocapacitance and the effective surface area. When plotted versus the OER current at a given overpotential (Figure 3.16), there is a linear trend, where the OER activity increases four to five times and is correlated with a factor of seven to eight increase in the pseudocapacitive cathodic charge passed. This lends some support to the claim that amorphization leads to an increase in the electrochemically active surface area. It should also be noted that on a per-volume basis the number of cobalt and iron ions present in the amorphous regions increases faster with region growth than the OER current, and thus not all of the transition metal cations are electrochemically available as active sites. These findings do not alter any previous claims of the high catalytic activity of BSCF82,¹⁰ where the activity was typically extracted from the second or third cycle where the amorphous layer is still thin. The maximum increase in electrochemically active surface area from such a layer is less than a factor of two. It has also been recently shown that related

cobalt perovskites can sustain OER activities even higher than BSCF82 without becoming amorphous.¹⁰⁶

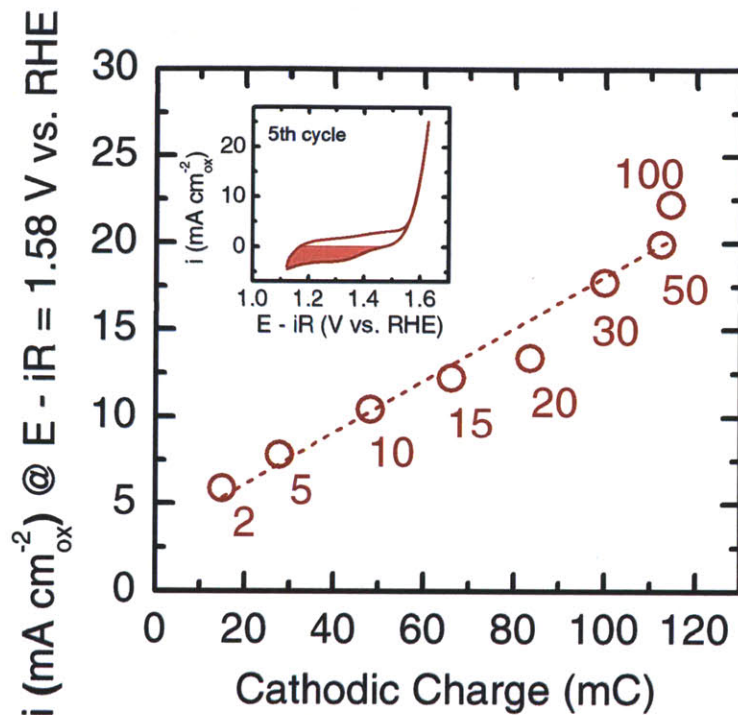


Figure 3.16: Oxygen evolution current at 1.58 V vs. RHE vs. the cathodic charge passed during a single cycle (1.1-1.7 V vs. RHE, 10 mV/s) in 0.1 M KOH. Cycle numbers are labeled. Inset shows a single cycle (5th) with the shaded region being proportional to the cathodic charge. Figure adapted from published work.¹¹

An interesting comparison arises when considering the highly active OER catalysts formed from electrodeposited cobalt oxide films. When normalizing the OER current of BSCF82 to the total number of cobalt atoms—taken as the lower limit of the intrinsic OER activity per cobalt—it was found to be comparable to that reported for the electrochemically deposited films,^{16,59,62,65} as shown in Figure 3.17. Recently it has been shown that the OER current per cobalt atom decreases with increasing “cluster” size of an extended cobalt oxide motif, which is a result of reduced utility of cobalt for OER.⁵⁷ Another recent report has investigated the local structures of the cobalt cations

via extended X-ray absorption fine structure (EXAFS), and has shown that during cycling, perovskite oxides BSCF82 and SCF82 both show an increase in the interatomic spacing associated with edge-shared cobalt octahedra, and begin to show similarity with the Fourier-transformed EXAFS of the electrochemically deposited amorphous cobalt oxide films.¹⁰⁷ Further investigation of the nature of the active sites in the amorphous regions of these perovskites and their relationship to the electrochemically deposited oxides is needed to obtain a fuller picture of how these catalysts function.

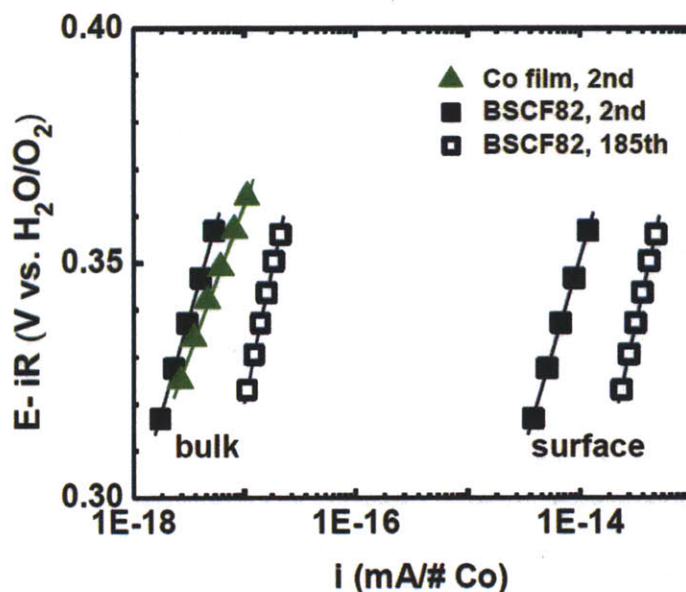


Figure 3.17: Tafel plots for BSCF82 (solid squares, 2nd cycle; open squares, 185th cycle) and an electrochemically-deposited amorphous Co oxide film (green triangle, 2nd cycle) in 0.1 M KOH. Tafel plots constructed from averaged forward-backward scans of cyclic voltammetry (10 mV/s) and normalized to the total number of Co in bulk or on the surface. BSCF82 data was gathered on a single electrode while the Co film data was the average of 5 independent measurements ($250 \text{ nmol/cm}^2_{\text{disk}}$ loading, 200 nm thick). The number of cobalt atoms in BSCF82 was estimated from the formula unit, mass loading and SEM-estimated surface area. For the Co-film, the number of Co ions was estimated from the Faradaic charge passed during electrodeposition at 0.806 V vs. SCE in 0.1 M potassium phosphate (pH 7), assuming all charge was due to Co^{2+} to Co^{3+} oxidation. Co film data was gathered by Marcel Risch. Figure adapted from published work.¹¹

3.6 O p -band Center: A Descriptor from Density Functional Theory

Thus far only the amorphization and its effect on catalytic activity have been discussed. In the following, a potential descriptor for OER activity and amorphization is reported based on density functional theory calculations. It has recently been reported that the oxygen p -band center, as calculated from density functional theory, acts as a descriptor for several physical parameters relating to oxygen anions in the perovskite structure such as the oxygen vacancy formation energy, oxygen mobility, and oxygen surface exchange coefficient.⁹⁶ This in turn leads the p -band center to describe the high temperature ORR activity of perovskite oxides as cathodes for solid oxide fuel cells. BSCF82, SCF82, and BSCF46 all have O p -band centers much closer to the Fermi level, allowing oxygen redox to occur more easily, leading to Fermi level pinning of the O p -band. The calculated O p -band centers for the oxides in this work, along with their OER overpotentials at $0.25 \text{ mA/cm}^2_{\text{ox}}$, are shown in Figure 3.18. Oxides with an O p -band center higher than approximately -2.2 eV relative to the Fermi level become amorphous during the OER in pH 13 electrolyte, while those with lower O p -band centers do not. Since LSC46 has an O p -band center at -2.2 eV , it is likely that an oxide at the threshold of becoming amorphous during OER has an O p -band center somewhere between that of LSC46 and SCF82. Indeed, there has been further study of the O p -band centers of related double-perovskite compounds that remain stable during OER with high activity, possessing O p -band centers of approximately -1.8 eV relative to the Fermi level.¹⁰⁶

Because a high O p -band center has been shown to provide higher oxygen lattice mobility and higher oxygen vacancy concentration in BSCF82,¹⁰⁸ BSCF46 and SCF82, changes in oxygen stoichiometry at the surface, whether from surface oxygen exchange or bulk vacancy migration, may play an important role in the amorphization process, or even in the OER mechanism itself. Further work is needed to understand the intimate relationship between lattice oxygen, structural stability and catalytic activity in alkaline solution.

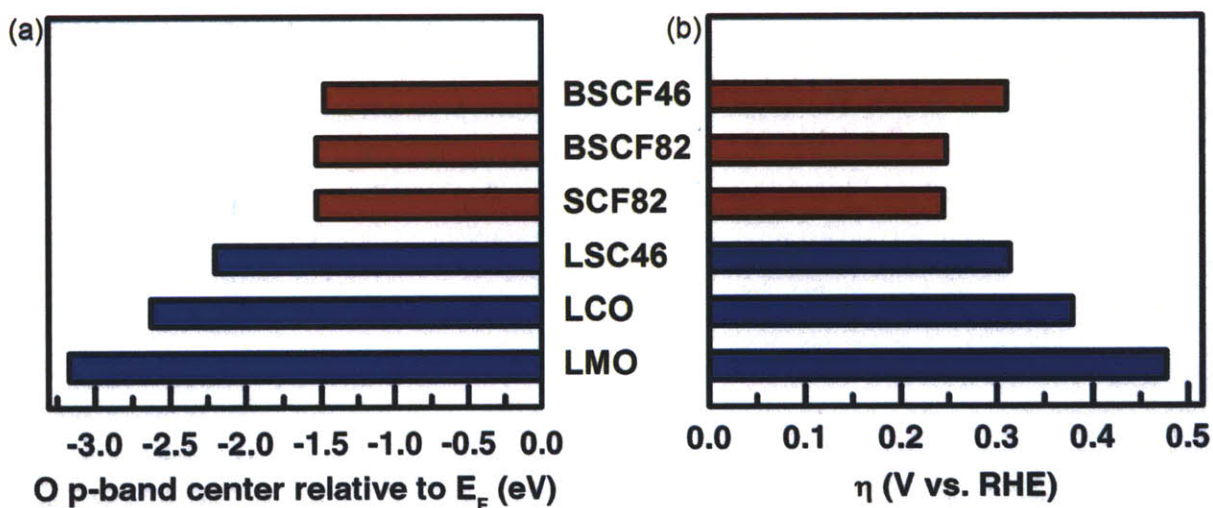


Figure 3.18: (a) Calculated O p -band centers of perovskites BSCF46, BSCF82, SCF82, LSC46, LCO and LMO, and (b) the overpotentials at $0.25 \text{ mA/cm}^2_{\text{ox}}$. Stoichiometry in the calculations is not exact due to the coarse composition grid in the simulated supercells. Oxides represented with red bars exhibit rapid surface amorphization during water oxidation, while those represented with blue bars remain highly crystalline. DFT performed by Yueh-Lin Lee. Figure adapted from published work.¹¹

4 Conclusions and Looking Forward

In this thesis, the amorphization of highly active BSCF82 and related compounds BSCF46 and SCF82 during OER was described. These oxides rapidly became amorphous at the surface when cycled in the OER potential region, with slower amorphization occurring for potentiostatically-held electrodes. Amorphization was accompanied by leaching of A-site cations from the surface and considerable increases in the pseudocapacitive and OER currents. Amorphization also led to the apparent atomic spacing of 2.8 Å from the ring observed in the FFTs of HRTEM images of the particle surfaces, indicating the possible formation of edge-sharing transition metal octahedra. All three of these oxides had similarly positioned O *p*-band centers as calculated by density functional theory, being the highest relative to the Fermi level compared to all the other oxides studied in this work. The perovskites LSC46, LCO and LMO, which had lower O *p*-band centers relative to the Fermi level, did not become amorphous and remained crystalline under identical electrochemical conditions.

There are several interesting research directions that arise from the results presented earlier. First is the parallel between the amorphous layer grown on BSCF82, BSCF46 and SCF82, and amorphous electrochemically-deposited cobalt films. Further work has recently been done via EXAFS on BSCF82, SCF82 and the amorphous films, showing that in the Fourier-transformed EXAFS interatomic distance peaks corresponding to Co-Co distances in edge-sharing octahedra appear and grow with electrochemical cycling in the OER region.¹⁰⁷ The possible similarity between the amorphous cobalt films and the amorphous layers formed on perovskites is what first

posed the question as to whether or not the perovskites' amorphous films were permeable to electrolyte, giving access to bulk cobalt as active sites for OER. It has already been reported that oxides formed on cobalt metal electrochemically are thought to be hydrous, and the film growth cyclic voltammetry shows an increase in both pseudocapacitance and OER current as the film becomes thicker.⁵¹ It had also been suggested that hydrous oxide films could be an example of three-dimensional catalysis, where the accessibility of bulk metal cation sites to electrolyte provide a higher electrochemically active surface area.^{47,109} Similar findings had also been reported for iridium oxide cycled in acidic solution.¹¹⁰⁻¹¹² Further experiments to determine whether or not the surface oxide films contain hydrous species such as hydroxide or oxyhydroxide and how far into a heavily amorphized film the hydrous species exist, are needed. Probing the subtle differences between different types of amorphous cobalt (or other transition metal) oxides, such as studying the effect of any remaining A-site cations in the amorphous layers, is also of interest to further understand how to optimize such materials for OER.

Another interesting point is the fact that currently, the most active cobalt-based oxide OER catalysts were primarily researched initially as high-temperature oxygen reduction cathode materials for solid-oxide fuel cells (SOFCs).^{113,114} It seems clear that the nature of the transition metal-oxygen bond is of vital importance for OER catalysis. Differential electrochemical mass spectrometry (DEMS) combined with isotope labeling of oxygen could be of interest in determining to what degree lattice oxygen participates in the OER. The degree to which oxygen vacancies are mobile in the bulk at room

temperature, and whether oxygen can be exchanged at the oxide-electrolyte interface could also be of interest to study, as changing oxygen stoichiometry locally near the surface could have profound effects on oxide stability and OER activity. Investigating the effects of pH and other electrolytes may also yield new insights. Overall, the many questions surrounding the interrelationship between lattice oxygen, OER activity, and oxide stability and its implications for permeability to electrolyte mean that there may be many nascent advances waiting to be made in the field of OER catalysis on oxides.

5 References

1. Birol, F. *World Energy Outlook 2011*. (Paris, 2011).
2. Conti, J., Holtberg, P. & Doman, L. E. *International Energy Outlook 2011*. (Washington, 2011).
3. Dincă, M., Surendranath, Y. & Nocera, D. G. Nickel-borate oxygen-evolving catalyst that functions under benign conditions. *Proceedings of the National Academy of Sciences of the United States of America* **107**, 10337 (2010).
4. Gray, H. B. Powering the planet with solar fuel. *Nature Chemistry* **1**, 7 (2009).
5. Lee, Y., Suntivich, J., May, K. J., Perry, E. E. & Shao-Horn, Y. Synthesis and Activities of Rutile IrO₂ and RuO₂ Nanoparticles for Oxygen Evolution in Acid and Alkaline Solutions. *The Journal of Physical Chemistry Letters* **3**, 399 (2012).
6. Lewis, N. S. & Nocera, D. G. Powering the planet: chemical challenges in solar energy utilization. *Proceedings of the National Academy of Sciences of the United States of America* **103**, 15729 (2006).
7. Kanan, M. W. & Nocera, D. G. In situ formation of an oxygen-evolving catalyst in neutral water containing phosphate and Co²⁺. *Science* **321**, 1072 (2008).
8. Trotochaud, L., Ranney, J. K., Williams, K. N. & Boettcher, S. W. Solution-Cast Metal Oxide Thin Film Electrocatalysts for Oxygen Evolution. *Journal of the American Chemical Society* **134**, 17253 (2012).
9. Smith, R. D. L. *et al.* Photochemical Route for Accessing Amorphous Metal Oxide Materials for Water Oxidation Catalysis. *Science* **340**, 60 (2013).
10. Suntivich, J., May, K. J., Gasteiger, H. A., Goodenough, J. B. & Shao-Horn, Y. A Perovskite Oxide Optimized for Oxygen Evolution Catalysis from Molecular Orbital Principles. *Science* **334**, 1383 (2011).
11. May, K. J. *et al.* Influence of Oxygen Evolution during Water Oxidation on the Surface of Perovskite Oxide Catalysts. *The Journal of Physical Chemistry Letters* **3**, 3264 (2012).
12. Zeng, K. & Zhang, D. Recent progress in alkaline water electrolysis for hydrogen production and applications. *Progress in Energy and Combustion Science* **36**, 307 (2010).
13. Choi, P. A simple model for solid polymer electrolyte (SPE) water electrolysis. *Solid State Ionics* **175**, 535(2004).
14. Rastan, E., Hagen, G. & Tunold, R. Electrocatalysis in water electrolysis with solid polymer electrolyte. *Electrochimica Acta* **48**, 3945 (2003).

15. Khaselev, O. & Turner, J. J. A. A Monolithic Photovoltaic-Photoelectrochemical Device for Hydrogen Production via Water Splitting. *Science* **280**, 425 (1998).
16. Dau, H. *et al.* The Mechanism of Water Oxidation: From Electrolysis via Homogeneous to Biological Catalysis. *ChemCatChem* **2**, 724 (2010).
17. Conway, B. & Salomon, M. Electrochemical reaction orders: Applications to the hydrogen- and oxygen-evolution reactions. *Electrochimica Acta* **9**, 1599 (1964).
18. Tseung, A. C. C. & Bevan, H. L. A reversible oxygen electrode. *Journal of Electroanalytical Chemistry and Interfacial Electrochemistry* **45**, 429 (1973).
19. Ruetschi, P. & Delahay, P. Influence of Electrode Material on Oxygen Overvoltage: A Theoretical Analysis. *The Journal of Chemical Physics* **23**, 556 (1955).
20. Hoar, T. P. The mechanism of the oxygen electrode. *Proceedings of the Royal Society of London. Series A, Containing Papers of a Mathematical and Physical Character* **142**, 628 (1933).
21. Damjanovic, A. Anodic Oxide Films as Barriers to Charge Transfer in O₂ Evolution at Pt in Acid Solutions. *Journal of The Electrochemical Society* **123**, 374 (1976).
22. Damjanovic, A. Electron transfer through thin anodic films in oxygen evolution at Pt electrodes in alkaline solutions. *Electrochimica Acta* **37**, 2533 (1992).
23. Bockris, J. O. Kinetics of Activation Controlled Consecutive Electrochemical Reactions: Anodic Evolution of Oxygen. *The Journal of Chemical Physics* **24**, 817 (1956).
24. Rossmeisl, J., Logadottir, A. & Nørskov, J. K. Electrolysis of water on (oxidized) metal surfaces. *Chemical Physics* **319**, 178 (2005).
25. Rossmeisl, J., Qu, Z. W., Zhu, H., Kroes, G. J. & Nørskov, J. K. Electrolysis of water on oxide surfaces. *Journal of Electroanalytical Chemistry* **607**, 83 (2007).
26. Man, I. C. *et al.* Universality in Oxygen Evolution Electrocatalysis on Oxide Surfaces. *ChemCatChem* **3**, 1159 (2011).
27. Azzam, A. M., Bockris, J. O., Conway, B. E. & Rosenberg, H. Some aspects of the measurement of hydrogen overpotential. *Transactions of the Faraday Society* **46**, 918 (1950).
28. Bockris, J. O. & Huq, A. K. M. S. The Mechanism of the Electrolytic Evolution of Oxygen on Platinum. *Proceedings of the Royal Society A: Mathematical, Physical and Engineering Sciences* **237**, 277 (1956).

29. Burke, L. D. & Moynihan, A. Oxygen electrode reaction. Part 1.—Nature of the inhibition process. *Transactions of the Faraday Society* **67**, 3550 (1971).
30. Visscher, W. & Devanathan, M. Anodic behavior of platinum electrodes in oxygen-saturated acid solutions. *Journal of Electroanalytical Chemistry* **8**, 127 (1964).
31. Riddiford, A. Mechanisms for the evolution and ionization of oxygen at platinum electrodes. *Electrochimica Acta* **4**, 170 (1961).
32. Hoare, J. P. The Reversible Oxygen Electrode. *Nature* **211**, 703 (1966).
33. Iwakura, C., Fukuda, K. & Tamura, H. The anodic evolution of oxygen on platinum oxide electrode in alkaline solutions. *Electrochimica Acta* **21**, 501 (1976).
34. Appleby, A. Rest potentials of oxide-free platinum electrodes. *Journal of Electroanalytical Chemistry and Interfacial Electrochemistry* **35**, 193 (1972).
35. Hoare, J. P. Oxygen Overvoltage Measurements on Bright Platinum in Acid Solutions. *Journal of The Electrochemical Society* **112**, 849 (1965).
36. Rand, D. A. J. & Woods, R. Cyclic voltammetric studies on iridium electrodes in sulphuric acid solutions. *Journal of Electroanalytical Chemistry and Interfacial Electrochemistry* **55**, 375 (1974).
37. Gambardella, A. A., Bjorge, N. S., Alspaugh, V. K. & Murray, R. W. Voltammetry of Diffusing 2 nm Iridium Oxide Nanoparticles. *The Journal of Physical Chemistry C* **115**, 21659 (2011).
38. Buckley, D. N. & Burke, L. D. The oxygen electrode. Part 6. —Oxygen evolution and corrosion at iridium anodes. *Journal of the Chemical Society, Faraday Transactions 1* **72**, 2431 (1976).
39. Burke, L. D. & O'Meara, T. O. Oxygen electrode reaction. Part 2. —Behaviour at ruthenium black electrodes. *Journal of the Chemical Society, Faraday Transactions 1* **68**, 839 (1972).
40. Beni, G., Schiavone, L. M., Shay, J. L., Dautremont-Smith, W. C. & Schneider, B. S. Electrocatalytic oxygen evolution on reactively sputtered electrochromic iridium oxide films. *Nature* **282**, 281 (1979).
41. Burke, L. D., Murphy, O. J., O'Neill, J. F. & Venkatesan, S. The oxygen electrode. Part 8.—Oxygen evolution at ruthenium dioxide anodes. *Journal of the Chemical Society, Faraday Transactions 1* **73**, 1659 (1977).
42. Ferrer, J. E. & Victori, L. Study of the oxygen evolution reaction on the iridium electrode in acid medium by eis. *Electrochimica Acta* **39**, 667 (1994).

43. Ferrer, J. E. & Victori, L. Oxygen evolution reaction on the iridium electrode in basic medium studied by electrochemical impedance spectroscopy. *Electrochimica acta* **39**, 581 (1994).
44. Nakagawa, T., Beasley, C. a. & Murray, R. W. Efficient Electro-Oxidation of Water near Its Reversible Potential by a Mesoporous IrO_x Nanoparticle Film. *The Journal of Physical Chemistry C* **113**, 12958 (2009).
45. Owe, L.-E., Tsytkin, M. & Sunde, S. The effect of phosphate on iridium oxide electrochemistry. *Electrochimica Acta* **58**, 231 (2011).
46. Owe, L.-E., Tsytkin, M., Wallwork, K., Haverkamp, R. G. & Sunde, S. Iridium-ruthenium single phase mixed oxides for oxygen evolution: Composition dependence of electrocatalytic activity. *Electrochimica Acta* **70**, 158 (2012).
47. Doyle, R. L. & Lyons, M. E. G. Kinetics and Mechanistic Aspects of the Oxygen Evolution Reaction at Hydrous Iron Oxide Films in Base. *Journal of the Electrochemical Society* **160**, H142 (2013).
48. Lyons, M. E. G. & Brandon, M. P. The oxygen evolution reaction on passive oxide covered transition metal electrodes in alkaline solution. Part III-Iron. *International Journal of Electrochemical Science* **3**, 1463 (2008).
49. Lyons, M. E. G. & Brandon, M. P. The oxygen evolution reaction on passive oxide covered transition metal electrodes in aqueous alkaline solution. Part 1-Nickel. *International Journal of Electrochemical Science* **3**, 1386 (2008).
50. Lyons, M. E. G. & Brandon, M. P. The oxygen evolution reaction on passive oxide covered transition metal electrodes in alkaline solution. Part 2-Cobalt. *International Journal of Electrochemical Science* **3**, 1425 (2008).
51. Burke, L., Lyons, M. & Murphy, O. Formation of hydrous oxide films on cobalt under potential cycling conditions. *Journal of Electroanalytical Chemistry and Interfacial Electrochemistry* **132**, 247 (1982).
52. Brossard, L. Cobalt black electrodes for the oxygen evolution reaction from electrolysis of 40 wt% KOH. *International Journal of Hydrogen Energy* **17**, 671 (1992).
53. Brossard, L. & Messier, C. Nickel coatings: deposition on an iron substrate and O₂ evolution in 40 wt.% KOH. *Materials Chemistry and Physics* **33**, 239 (1993).
54. Jones, E. & Wynne-Jones, W. F. K. The nickel oxide electrode. Part 2. *Transactions of the Faraday Society* **52**, 1260 (1956).
55. Conway, B. E. & Bourgault, P. L. The Electrochemical Behavior of the Nickel-Nickel Oxide Electrode: Part I. Kinetics of Self-Discharge. *Canadian Journal of Chemistry* **37**, 292 (1959).

56. Hickling, A. & Hill, S. Oxygen overvoltage. Part I. The influence of electrode material, current density, and time in aqueous solution. *Discussions of the Faraday Society* **1**, 236 (1947).
57. Risch, M. *et al.* Water Oxidation by Electrodeposited Cobalt Oxides-Role of Anions and Redox-Inert Cations in Structure and Function of the Amorphous Catalyst *ChemSusChem* **5**, 542 (2012).
58. Risch, M. *et al.* Atomic structure of cobalt-oxide nanoparticles active in light-driven catalysis of water oxidation. *International Journal of Hydrogen Energy* **37**, 8878 (2012).
59. Esswein, A. J., Surendranath, Y., Reece, S. Y. & Nocera, D. G. Highly active cobalt phosphate and borate based oxygen evolving catalysts operating in neutral and natural waters. *Energy & Environmental Science* **4**, 499 (2011).
60. Bediako, D. K. *et al.* Structure-Activity Correlations in a Nickel-Borate Oxygen Evolution Catalyst. *Journal of the American Chemical Society* **134**, 6801 (2012).
61. Bediako, D. K., Surendranath, Y. & Nocera, D. G. Mechanistic Studies of the Oxygen Evolution Reaction Mediated by a Nickel-Borate Thin Film Electrocatalyst. *Journal of the American Chemical Society* **135**, 3662 (2013).
62. Surendranath, Y., Kanan, M. W. & Nocera, D. G. Mechanistic studies of the oxygen evolution reaction by a cobalt-phosphate catalyst at neutral pH. *Journal of the American Chemical Society* **132**, 16501 (2010).
63. Risch, M. *et al.* Cobalt-oxo core of a water-oxidizing catalyst film. *Journal of the American Chemical Society* **131**, 6936 (2009).
64. Risch, M. *et al.* Characterisation of a water-oxidizing Co-film by XAFS. *Journal of Physics: Conference Series* **190**, 012167 (2009).
65. Kanan, M. W. *et al.* Structure and valency of a cobalt-phosphate water oxidation catalyst determined by in situ X-ray spectroscopy. *Journal of the American Chemical Society* **132**, 13692 (2010).
66. Balandin, A. A. Modern State of the Multiplet Theory of Heterogeneous Catalysis. *Advances in Catalysis* **19**, 1 (1969).
67. Sabatier, P. Hydrogénations et déshydrogénations par catalyse. *Berichte der deutschen chemischen Gesellschaft* **44**, 1984 (1911).
68. Trasatti, S. Electrocatalysis by oxides-Attempt at a unifying approach. *Journal of Electroanalytical Chemistry* **111**, 125 (1980).
69. Koper, M. T. M. Thermodynamic theory of multi-electron transfer reactions: Implications for electrocatalysis. *Journal of Electroanalytical Chemistry* **660**, 254 (2011).

70. Wolfram, T. & Ellialtıođlu, Ő. *Electronic and Optical Properties of d-Band Perovskites*. (Cambridge University Press: New York, 2006).
71. Peña, M. a. & Fierro, J. L. G. Chemical Structures and Performance of Perovskite Oxides. *Chemical Reviews* **101**, 1981 (2001).
72. Bockris, J. O. M. & Otagawa, T. The electrocatalysis of oxygen evolution on perovskites. *Journal of the Electrochemical Society* **131**, 290 (1984).
73. Bockris, J. O. M. & Otagawa, T. Mechanism of oxygen evolution on perovskites. *The Journal of Physical Chemistry* **87**, 2960 (1983).
74. Bockris, J. O. M., Otagawa, T. & Young, V.- Solid state surface studies of the electrocatalysis of oxygen evolution on perovskites. *Journal of Electroanalytical Chemistry and Interfacial Electrochemistry* **150**, 633 (1983).
75. Otagawa, T. Lanthanum Nickelate as Electrocatalyst: Oxygen Evolution. *Journal of The Electrochemical Society* **129**, 2391 (1982).
76. Suntivich, J. *et al.* Design principles for oxygen-reduction activity on perovskite oxide catalysts for fuel cells and metal-air batteries. *Nature Chemistry* **3**, 546 (2011).
77. Tejuca, L. G., Fierro, J. L. G. & Tasc3n, J. M. D. Structure and Reactivity of Perovskite-Type Oxides. *Advances in Catalysis* **36**, 237 (1989).
78. Cox, P. A. *Transition Metal Oxides: An Introduction to their Electronic Structure and Properties*. (Oxford University Press: New York, 1992).
79. Matsumoto, Y., Yoneyama, H. & Tamura, H. Electrochemical properties of lanthanum nickel oxide. *Journal of Electroanalytical Chemistry and Interfacial Electrochemistry* **80**, 115 (1977).
80. Matsumoto, Y., Kurimoto, J. & Sato, E. Oxygen evolution on SrFeO₃ electrode. *Journal of Electroanalytical Chemistry* **102**, 77 (1979).
81. Matsumoto, Y. Oxygen Evolution on La_{1-x}Sr_xFe_{1-y}Co_yO₃ Series Oxides. *Journal of The Electrochemical Society* **127**, 2360 (1980).
82. Matsumoto, Y. & Sato, E. Oxygen evolution on La_{1-x}Sr_xMnO₃ electrodes in alkaline solutions. *Electrochimica Acta* **24**, 421 (1979).
83. Matsumoto, Y. Oxygen Evolution on La_{1-x}Sr_xCoO₃ Electrodes in Alkaline Solutions. *Journal of The Electrochemical Society* **127**, 811 (1980).
84. Hammer, B. Electronic factors determining the reactivity of metal surfaces. *Surface Science* **343**, 211 (1995).

85. Hammer, B. Special Sites at Noble and Late Transition Metal Catalysts. *Topics in Catalysis* **37**, 3 (2006).
86. Crumlin, E. J. *et al.* Surface Strontium Enrichment on Highly Active Perovskites for Oxygen Electrocatalysis in Solid Oxide Fuel Cells. *Energy & Environmental Science* **5**, 6081 (2012).
87. Ferreira, P. J. *et al.* Instability of Pt/C Electrocatalysts in Proton Exchange Membrane Fuel Cells. *Journal of The Electrochemical Society* **152**, A2256 (2005).
88. Suntivich, J., Gasteiger, H. A., Yabuuchi, N. & Shao-Horn, Y. Electrocatalytic Measurement Methodology of Oxide Catalysts Using a Thin-Film Rotating Disk Electrode. *Journal of the Electrochemical Society* **157**, B1263 (2010).
89. Kresse, G. & Hafner, J. Ab initio molecular dynamics for liquid metals. *Physical Review B* **47**, 558 (1993).
90. Kresse, G. & Furthmüller, J. Efficient iterative schemes for ab initio total-energy calculations using a plane-wave basis set. *Physical Review B* **54**, 11169 (1996).
91. Blöchl, P. E. Projector augmented-wave method. *Physical Review B* **50**, 17953 (1994).
92. Perdew, J. P. & Wang, Y. Accurate and simple analytic representation of the electron-gas correlation energy. *Physical Review B* **45**, 13244 (1992).
93. Anisimov, V. I., Aryasetiawan, F. & Lichtenstein, A. I. First-principles calculations of the electronic structure and spectra of strongly correlated systems: the LDA + U method. *Journal of Physics: Condensed Matter* **9**, 767 (1997).
94. Dudarev, S. L., Savrasov, S. Y., Humphreys, C. J. & Sutton, A. P. Electron-energy-loss spectra and the structural stability of nickel oxide: An LSDA+U study. *Physical Review B* **57**, 1505 (1998).
95. Lee, Y.-L., Kleis, J., Rossmeisl, J. & Morgan, D. Ab initio energetics of LaBO₃ (001) (B=Mn, Fe, Co, and Ni) for solid oxide fuel cell cathodes. *Physical Review B* **80**, 224101 (2009).
96. Lee, Y.-L., Kleis, J., Rossmeisl, J., Shao-Horn, Y. & Morgan, D. Prediction of solid oxide fuel cell cathode activity with first-principles descriptors. *Energy & Environmental Science* **4**, 3966 (2011).
97. Wei, S.-H., Ferreira, L., Bernard, J. & Zunger, A. Electronic properties of random alloys: Special quasirandom structures. *Physical Review B* **42**, 9622 (1990).
98. Hertz, J. *et al.* Magnetism and structure of Li_xCoO₂ and comparison to Na_xCoO₂. *Physical Review B* **77**, 1 (2008).

99. Miyazaki, S., Kikkawa, S. & Koizumi, M. Chemical and electrochemical deintercalations of the layered compounds LiMO_2 ($M = \text{Cr, Co}$) and $\text{NaM}'\text{O}_2$ ($M' = \text{Cr, Fe, Co, Ni}$). *Synthetic Metals* **6**, 211 (1983).
100. Arnold, M., Gesing, T. M., Martynczuk, J. & Feldhoff, A. Correlation of the Formation and the Decomposition Process of the BSCF Perovskite at Intermediate Temperatures. *Chemistry of Materials* **20**, 5851 (2008).
101. Zhang, W., Wang, Z. & Chen, X. M. Crystal structure evolution and local symmetry of perovskite solid solution $\text{Ba}[(\text{Fe}_{1/2}\text{Nb}_{1/2})_{1-x}\text{Ti}_x]\text{O}_3$ investigated by Raman spectra. *Journal of Applied Physics* **110**, 064113 (2011).
102. Ishikawa, a., Nohara, J. & Sugai, S. Raman Study of the Orbital-Phonon Coupling in LaCoO_3 . *Physical Review Letters* **93**, 1 (2004).
103. Gerken, J. B. *et al.* Electrochemical water oxidation with cobalt-based electrocatalysts from pH 0-14: the thermodynamic basis for catalyst structure, stability, and activity. *Journal of the American Chemical Society* **133**, 14431 (2011).
104. Risch, M. *et al.* Nickel-oxido structure of a water-oxidizing catalyst film. *Chemical communications (Cambridge, England)* **47**, 11912 (2011).
105. Zaharieva, I. *et al.* Synthetic manganese-calcium oxides mimic the water-oxidizing complex of photosynthesis functionally and structurally. *Energy & Environmental Science* **4**, 2400 (2011).
106. Grimaud, A. *et al.* Double Perovskites as a New Family of Highly Active Catalysts For Oxygen Evolution in Alkaline Solution. *Submitted*
107. Risch, M. *et al.* Structural Changes of Cobalt-Based Perovskites upon Water Oxidation Investigated by EXAFS. *The Journal of Physical Chemistry C* **117**, 8628 (2013).
108. McIntosh, S., Vente, J., Haije, W., Blank, D. & Bouwmeester, H. Structure and oxygen stoichiometry of $\text{SrCo}_{0.8}\text{Fe}_{0.2}\text{O}_{3-\delta}$ and $\text{Ba}_{0.5}\text{Sr}_{0.5}\text{Co}_{0.8}\text{Fe}_{0.2}\text{O}_{3-\delta}$. *Solid State Ionics* **177**, 1737 (2006).
109. Burke, L. D. & O'Sullivan, E. J. M. Oxygen gas evolution on hydrous oxides — An example of three-dimensional electrocatalysis? *Journal of Electroanalytical Chemistry and Interfacial Electrochemistry* **117**, 155 (1981).
110. Buckley, D. N., Burke, L. D. & Mulcahy, J. K. The oxygen electrode. Part 7.— Influence of some electrical and electrolyte variables on the charge capacity of iridium in the anodic region. *Journal of the Chemical Society, Faraday Transactions 1* **72**, 1896 (1976).

111. Buckley, D. N. & Burke, L. D. The oxygen electrode. Part 5.—Enhancement of charge capacity of an iridium surface in the anodic region. *Journal of the Chemical Society, Faraday Transactions 1* **71**, 1447 (1975).
112. McIntyre, J. D. E. Oxidation State Changes and Structure of Electrochromic Iridium Oxide Films. *Journal of The Electrochemical Society* **127**, 1264 (1980).
113. Wang, L., Merkle, R. & Maier, J. Surface Kinetics and Mechanism of Oxygen Incorporation Into $\text{Ba}_{1-x}\text{Sr}_x\text{Co}_y\text{Fe}_{1-y}\text{O}_{3-\delta}$ SOFC Microelectrodes. *Journal of The Electrochemical Society* **157**, B1802 (2010).
114. Kuroda, C., Zheng, K. & Świerczek, K. Characterization of novel $\text{GdBa}_{0.5}\text{Sr}_{0.5}\text{Co}_{2-x}\text{Fe}_x\text{O}_{5+\delta}$ perovskites for application in IT-SOFC cells. *International Journal of Hydrogen Energy* **8**, 1 (2012).